

Upcycled Synthesis and Extraction of Carbon-Encapsulated Iron Carbide Nanoparticles for Gap Plasmon Applications in Perovskite Solar Cells

Jiye Han¹, Kyusun Kim¹, Mohammad Tavakkoli², Jongmin Lee³, Dawoon Kim⁴, In Chung⁴, Aram Lee⁵, Keonwoo Park¹, Yongping Liao², Jin-Wook Lee¹, Seoung-Ki Lee⁵, Jin-Woo Oh⁶, Hyokyung Sung⁷, Esko Kauppinen², and IL JEON¹

¹Sungkyunkwan University

²Aalto University School of Science

³Hallym University

⁴Seoul National University

⁵Korea Institute of Science and Technology

⁶Pusan National University

⁷Kookmin University

December 13, 2022

Abstract

An effective method for obtaining large amounts of metal nanoparticles encapsulated by carbon layers through upcycling from floating-catalyst aerosol chemical vapor deposited carbon nanotubes is demonstrated. Nanoparticles with diameters of less than 20 μm are selectively extracted from the synthesized carbon assortments through sonication, centrifugation, and filtration. The particles show an aggregation behavior owing to the π - π interaction between the graphitic carbon shells surrounding the iron carbides. By controlling the degree of the aggregation and arrangement, the light scattering by the gap-surface plasmon effect in perovskite solar cells is maximized. Application of the nanoparticles to the devices increased the power conversion efficiency from 19.71% to 21.15%. The short-circuit current density (JSC) trend over the particle aggregation time accounts for the plasmonic effect. The devices show high stability analogue to the control devices, confirming that no metal-ion migration took place thanks to the encapsulation.

Upcycled Synthesis and Extraction of Carbon-Encapsulated Iron Carbide Nanoparticles for Gap Plasmon Applications in Perovskite Solar Cells

Jiye Han, Kyusun Kim, Mohammad Tavakkoli, Jongmin Lee, Dawoon Kim, In Chung, Aram Lee, Keonwoo Park, Yongping Liao, Jin-Wook Lee, Seoung-Ki Lee, Hyokyung Sung*, Esko Kauppinen*, Il Jeon*

Dr. J. Han, Dr. K. Kim, K.W. Park, Prof. J.-W. Lee, Prof. I. Jeon
Department of Nano Engineering, SKKU Advanced Institute of Nanotechnology (SAINT),
Sungkyunkwan University (SKKU), Suwon 16419, Republic of Korea

M. Tavakkoli, Dr. Y. Liao, E. Kauppinen,
Department of Applied Physics, School of Science Aalto University, Aalto 15100, Finland

Prof. J.M. Lee
School of Nano Convergence Technology, Hallym University, Chuncheon, Gangwon-do,
24252, Republic of Korea

D.W. Kim, I. Chang
School of Chemical and Biological Engineering, and Institute of Chemical Processes, Seoul
National University, Seoul 08826, Republic of Korea

A.R. Lee, Prof. S.-K. Lee
Institute of Advanced Composite Materials, Korea Institute of Science and Technology
(KIST), Jeollabuk-do 55324 Republic of Korea

Prof. S.-K. Lee
Department of Materials Science and Engineering, Pusan National University, Busan 46241,
Republic of Korea

Prof. H.K. Sung
Department of Materials Science and Engineering, Kookmin University, Seoul 02707,
Republic of Korea

E-mail: il.jeon@spc.oxon.org, esko.kauppinen@aalto.fi, hyokyung@kookmin.ac.kr

Keywords: iron nanoparticles, carbon nanoparticles, carbon encapsulation, carbon nanotubes,
perovskite solar cells, plasmonic effect

An effective method for obtaining large amounts of metal nanoparticles encapsulated by carbon layers through upcycling from floating-catalyst aerosol chemical vapor deposited carbon nanotubes is demonstrated. Nanoparticles with diameters of less than 20 μm are selectively extracted from the synthesized carbon assortments through sonication, centrifugation, and filtration. The particles show an aggregation behavior owing to the π - π interaction between the graphitic carbon shells surrounding the iron carbides. By controlling the degree of the aggregation and arrangement, the light scattering by the gap-surface plasmon effect in perovskite solar cells is maximized. Application of the nanoparticles to the devices increased the power conversion efficiency from 19.71% to 21.15%. The short-circuit current density (J_{SC}) trend over the particle aggregation time accounts for the plasmonic effect. The devices show high stability analogue to the control devices, confirming that no metal-ion migration took place thanks to the encapsulation.

1. Introduction

In the context of an environmentally sustainable society, organometallic halide perovskite solar cells (PSCs) have emerged as promising next-generation thin-film solar cells.¹⁻⁴ This is owing to the exceptionally high power conversion efficiency (PCE) of PSCs, as the reported certified efficiency is 25.6%.⁵⁻⁸ To achieve a high PCE, many efforts have been made by researchers globally. Conventionally, a strategy for testing various compositions of perovskites by changing the precursor ratio to adjust the perovskite film bandgap has been reported.⁹⁻¹³ A more contemporary strategy is to use additives in PSCs. Additive materials, such as polymers,^{14,15} small molecules,^{16,17} nanocarbons,¹⁸⁻²⁰ and even biomaterials,²¹ have been proven to be effective in increasing the device performance of PSCs by enlarging the perovskite crystals and passivating interfacial defects.²²⁻²⁴ Such an additive approach is an attractive method because small amounts of materials entailed by a facile process have a tremendous impact on the PSC performance. Another well-established additive approach is the insertion of

metal nanoparticles (NPs) to stimulate light absorption via the plasmonic effect.²⁵ NPs^{26–29} have been utilized in various fields, including biomedicine,³⁰ batteries,³¹ and photovoltaics. The nanoscale size of NPs induces quantum effects, opening up infinite possibilities when employed in devices. Metal NPs are unique among a wide range of NPs, as they can induce optical enhancement via plasmonic effects^{32–36} and effective charge extraction by a host–guest electronic interaction.^{37–40} A large number of electrons participate in the surface plasmonic resonance, improving the proximity field at the intrinsic frequency of the plasmonic metal NPs.^{41,42} Thin-film solar cells such as organic solar cells^{43–46} and PSCs^{47–50} have exploited the properties of metal NPs to boost their PCE. However, it should be emphasized that applications of metal NP in PSCs are much fewer than those in organic solar cells. This is ascribed to the ion-migration-derived degradation of metal halide perovskite materials.^{51–54} Inserting metal NPs within the PSC device system or, even worse, directly next to the perovskite layer, results in degradation of the PSCs. Higgins *et al.* and Yao *et al.* suggested a solution to this, that is, protecting NPs by carbon materials, using which they increased the PCE of PSCs while retaining device stability.^{34,38} To date, two types of carbon-encapsulated metal NPs have been reported, namely, metallofullerenes and carbon-encapsulated iron carbide (FeC@C). FeC@C NPs were generated by heating ferrocene particles with carbon allotropes under high pressure.^{37,62} In contrast to metallofullerenes, which are produced by inserting metal species into the fullerene cage,^{55–58} FeC@C is synthesized by growing carbon from the iron (Fe) core.^{59–64} The FeC in FeC@C has an Fe/Fe_{1-x}C_x core/shell structure encapsulated by several carbon layers.^{59,63} This is simpler and incurs a much lower production cost and higher yield compared to metallofullerene synthesis.

In this study, we propose a facile and eco-friendly upcycling method of producing FeC@C NPs and demonstrate their applicability in photovoltaic devices as plasmonic NPs. Aerosol-synthesized carbon nanotubes (CNTs) use ferrocene as a catalyst.^{65–67} As a result, the produced CNT films inevitably contain FeC@C NPs, which are regarded as impurities by CNT

researchers. Unsuccessful synthesis leaves excess amounts of FeC@C NPs in CNT films, lowering the electrical performance of the CNTs. Instead of treating this as a failed CNT sample, FeC@C NPs can be selectively collected from the CNTs. Accordingly, a method of extracting FeC@C NPs from aerosol-synthesized CNTs is introduced in this work along with their application to PSCs as plasmonic light and charge transport enhancers that do not induce ion migration. FeC@C NPs with a diameter of *ca.* 5–20 nm were extracted via sonication, centrifugation, and filtration. The collected NPs exhibited a fascinating trait of aggregation over time, which was attributed to the π – π interaction between the surrounding graphitic carbon layers, as observed from various analyses. By controlling the aggregation time, the gap plasmon coupling between the constituent NPs produced diverse plasmon modes, providing freedom to manipulate the optical properties via different nano-assemblies.⁶⁸ This was supported by optical measurements and computational analyses. To exploit this phenomenon, the FeC@C NP solution was drop-cast onto the SnO₂ layer or onto the fluorine-doped tin oxide (FTO) layer, followed by certain periods of waiting time for aggregation to occur before the subsequent PSC fabrication. The FeC@C NP-added PSCs showed a considerably improved device performance compared to the control devices, irrespective of the FeC@C NPs above the SnO₂ layer or FTO layer. The aggregation waiting time of 3 h was optimal, giving the highest PCE of 21.15% and 20.57% from the PSCs with the NPs on SnO₂ and FTO, respectively. This is a substantial increase as the control PSCs without NPs gave a PCE of 19.71%. The increasing trend of short-circuit current density (J_{sc}) with the waiting time for NP aggregation revealed that the improved PCE resulted from the gap-surface plasmonic effect of the aggregated NPs. Enhanced electron collection by the inserted FeC@C NPs contributed to the increase in open-circuit voltage (V_{oc}) and fill factor (FF), which was corroborated by the investigation carried out herein. We conclude that the addition of FeC@C NPs induced not only the gap-surface plasmon effect but also favorable charge transport. The location of the added FeC@C NPs in the PSCs did not affect the device performance on SnO₂ or FTO. The unencapsulated FeC@C NP-added PSCs

exhibited stable operation for over 40 days under ambient conditions compared to the control devices, confirming that no ion migration occurs and the use of NPs does not damage the perovskite layer. This is the first demonstration of carbon-encapsulated metal nanoparticles used as gap-surface plasmons in device applications. The proposed novel approach is a versatile and cost-effective route which does not promote metal ion migration and will therefore lead to a breakthrough in the field of nanoparticle-based next-generation optoelectronics.

2. Results and Discussion

2.1. Upcycled Synthesis of Carbon-Encapsulated Iron Nanoparticles

2.1.1. Synthesis of Carbon-Encapsulated Iron Carbide Nanoparticles

Carbon films containing a large proportion of FeC@C NPs were synthesized using the floating-catalyst aerosol chemical vapor deposition under a specific condition described in the experimental section. The produced carbon films were observed using high-resolution transmission electron microscopy (HR-TEM) (**Figure. 1a**). Expectedly, a large amount of FeC@C NPs was attached to the surface of the CNT strands. Energy-dispersive X-ray spectroscopy (EDS) analysis of TEM was used to identify FeC@C NPs by focusing on one of the CNT strands (**Figure. 1b** and **S1**). The presence of Fe along the CNT strand confirmed the existence of FeC@C NPs. The HR-TEM image of the carbon film shows that FeC@C NPs have diameters between 5 nm and 20 nm (**Figure. S2**). NPs with a diameter of ~8 nm were predominant, and they appeared completely wrapped by several layers of carbon sheets (**Figure. S2b**). X-ray photoelectron spectroscopy (XPS) was used to ascertain the identity of the FeC@C NPs by probing the elemental status before and after cleaning the carbon films with acid (**Figure. 1c-g** and **S3**). In this XPS analysis, we introduced conventional CNT films as well for comparison. The intensity of the Fe_{2p3}, Fe_{3p}, and Fe_{2p} peaks from the aerosol-synthesized carbon

film were considerably greater than those from the conventionally synthesized CNT films in which ferrocene was also used as the catalyst (**Figure. 1c** and **S3**). To prove that the produced Fe NPs were thoroughly encapsulated by the carbon sheet, we rinsed the carbon film with triflic acid (TFMS). The intensity of the C_{1s} peak decreased after the acid treatment, from which we can deduce that any remaining unencapsulated FeO along with carbon impurities were washed away (**Figure. 1d**).^{69,70} The fact that the intensity of the Fe peaks is stronger after the acid treatment indicates the reduction of FeO (**Figure. 1e** and **S3b**). The FeC@C NPs were completely encapsulated by the carbon sheet, therefore unaffected by the acid, as evidenced by the conspicuous Fe peaks. The disappearance of the O_{1s} shoulder at 530 eV indicates the removal of oxygen from FeO, which supports our claim (**Figure. 1f**).^{71,72} The overall O_{1s} peak at 534 eV increased in intensity after the acid treatment, probably due to the hygroscopic TFMS-doped carbon films attracting H_2O and O_2 .

2.1.2. Extraction of Carbon-Encapsulated Iron Carbide Nanoparticles

As the next step, FeC@C NPs were separated from the aerosol-synthesized carbon films by ultrasonication and filtration (**Figure. 2a**). The separation procedure was as follows (**Figure. 2b**): a carbon film containing a large amount of FeC@C-attached CNTs was sonicated intensively for 6 h in chlorobenzene (CB) to separate as many NPs as possible from the CNTs (**Figure. S4**). The FeC@C NPs dispersed in CB showed magnetic properties, confirming the presence of FeC (**Figure. S5** and **Video 1**).^{73–75} The solution was centrifuged at 10,000 rpm for 20 min to sink large-size FeC@C NPs and CNTs. The supernatant of the solution was filtered by polytetrafluoroethylene (PTFE) with a 0.20- μ m pore size to remove further impurities. The effects of sonication and filtration were analyzed using dynamic light scattering (DLS). The DLS data shows that the sonicated solution contains NPs with different sizes as well as some CNTs (**Figure. 2c** and **S6a**); NPs with a size of *ca.* 10 nm were dominant according to the DLS

number graph (**Figure. 2d** and **S6a**). This matches the size of the individual FeC@C NPs observed in the HR-TEM images (Figure. S2). Remeasuring the same solution after a few hours of waiting did not show any peaks, indicating that the NPs and CNTs had sunk down below the detection range (**Figure. S6b**). Interestingly, the measurement of the same solution after giving a gentle swirl showed the NP peaks but with an increased size, revealing that aggregation of NPs might have occurred owing to the π - π interaction between the graphitic carbon shells (**Figure. S6c**). Further waiting increased the NP size even greater (**Figure. 2c, 2d, and S6d**). The DLS data of the filtered solution showed that any particles greater than 100 nm, including CNTs, were removed (**Figure. 2d** and **S7**). This means that we can control the size and degree of the FeC@C NP aggregation by waiting before drop-casting a NP solution onto a substrate. To confirm this, we used atomic force microscopy (AFM) and TEM. The FeC@C NPs were uniformly coated on a glass substrate according to the AFM images (**Figure. S8**). However, the resolution of the images were not enough to observe NP aggregation. To verify the aggregation over the waiting time, we prepared FeC@C NPs on an HR-TEM grid according to the waiting time. We observed that some of the FeC@C NPs aggregated (**Figure. 2e**), and the aggregation became stronger with the waiting time (**Figure. 2f**). Despite our attempt to substantiate the π - π interaction between the carbon shells of the FeC@C NPs using the XPS technique, the quantity of FeC@C NPs coated on substrates was too low, and the Fe component was not detectable (**Figure. S9**).

2.2. Controlled Aggregation of Carbon-Encapsulated Iron Nanoparticles

2.2.1. Plasmonic Effect of Aggregated Carbon-Encapsulated Iron Carbide Nanoparticles

The controlled aggregation of the FeC@C NPs with fixed gaps between the NPs indicated that a powerful optical effect could be induced. This can lead to a remarkable improvement in photon absorption when exploited in device applications such as PSCs. To examine this, we conducted ultraviolet–visible (UV–Vis) absorption spectroscopy on the aggregated FeC@C NPs under different waiting time. The data show that the extinction increases with an increase in the waiting time (**Figure. 3a**) and decreases back when the waiting time exceeds 3 h (**Figure. 3b**). This is a typical indication of the plasmonic effect caused by NPs.^{76–79} This phenomenon was investigated further using computational analysis. We modelled a spherical Fe core surrounded by a thin layer of C shell with varying diameters of Fe NP (D) and varying thickness of the C shell (t). The core diameter and the C shell thickness variables were set as 5, 10, and 15 nm, based on the information from the TEM images (Figure. S2), and as 0, 1, 2, and 3 nm based on the reported multilayer graphene thickness (**Table S1**), respectively (**Figure. 3c** and **S10**).^{80,81} The absorption and scattering cross-sections were calculated based on the varying core diameter and shell thickness, as well as different NP arrangements simulating NP aggregation (**Figure. 3d** and **S11**). It was postulated that the scattering is favorable for the light absorption of the perovskite active film; however, the absorption of NPs themselves undermines the plasmonic enhancement. Thus, obtaining the conditions where the absorption cross-section is minimal and the scattering cross-section is maximum is important. According to the simulation results, a single FeC@C NP has absolutely no optical effect, regardless of the size (**Figure. S12** and **S13**). However, the aggregated FeC@C NPs showed substantial scattering, despite a relatively small increase in absorption. In fact, the degree of absorption reverses when the number of aggregated NPs exceeds 4–5, whereas the degree of scattering increases continuously (**Figure. 3d**). This indicates that the larger the aggregation, the greater is the plasmonic effect. Therefore, the gap plasmonic effect is a dominant factor in the near-field light absorption enhancement by the FeC@C NPs, and the shell thickness is a key parameter in determining the amount of generated plasmonic polaritons

when electromagnetic fields are coupled with plasmons.⁸² With an increase in the shell thickness, the scattering cross-section red-shifts from *ca.* 500 nm to 700 nm, which is within the effective absorption range of the perovskite photoactive films.^{83,84} The shell thickness was deduced to be approximately 1 nm with 2–3 graphitic layers in the TEM images (**Figure. S2** and **Table S1**). Hence, we assume the shell thickness, t , to be 1, which produces a strong scattering cross-section (**Figure. 3e**) and gap-surface plasmon-induced electric field (**Figure. 3f**) for all three core sizes, D . Raman spectroscopy was also performed on drop-cast FeC@C NPs on glass substrates according to the waiting time to confirm the plasmonic effect. (**Figure. S14**). The Raman peak intensity and band positions depend on the conditions of the carbon nanostructure.⁸⁵ The difference in the Raman signal intensity for each excitation wavelength of the laser, namely 532 nm, 633 nm, and 785 nm, serves as indirect evidence for the electromagnetic field enhancement profile.⁸⁶ At laser wavelengths of 532 nm and 633 nm, the Raman signal intensity of the D+D' band ($\sim 3000\text{ cm}^{-1}$) was greater than that of the D band ($\sim 1500\text{ cm}^{-1}$). However, at 785 nm, the intensity of the D band intensified as the intensity of the D + D' band decreased in all samples with different waiting times. This evidences the plasmonic effect in which the calculated scattering cross-section value decreases with an increase in the wavelength of the incident light. To our dismay, variation in the Raman intensity over the waiting time was not observed. This means that the surface enhanced Raman scattering (SERS) effect witnessed here is originated perhaps from the charge transfer mechanism of host–guest interaction within the NPs more than the electromagnetic mechanism, the latter of which corresponds to the localized surface plasmonic resonance.^{87–89} As the electromagnetic mechanism-driven SERS effect arises from the nanoscale gaps between NPs, aggregation of FeC@C NPs is a key contributing factor.

2.3. Perovskite Solar Cell Application of Carbon-Encapsulated Iron Nanoparticles

$\text{Cs}_{0.05}\text{FA}_{0.80}\text{MA}_{0.15}\text{PbI}_{2.75}\text{Br}_{0.25}$ -based PSCs were fabricated in the configurational structure of FTO/SnO₂/perovskite/spiro-MeOTAD/Au, where the FeC@C NPs were drop-cast onto FTO layers or SnO₂ layers (**Figure. 4a** and **4b**). The top-view SEM images show that the quality of the perovskite films was similar for both cases; however, the perovskite films formed on pristine SnO₂ showed a marginally larger crystal domain size than the perovskite films formed on the FeC@C NP-deposited SnO₂ (**Figure. 4c** and **4d**). We suspect that the presence of FeC@C NPs on SnO₂ may hinder the growth of the perovskite film, even though the FeC@C NPs were not visible in the cross-sectional SEM images (**Figure. 4e** and **4f**). EDS was performed on the same device. However, as the amount of FeC@C NP was too low to be detectable from the cross-sectional images (**Figure. S15**). The devices were fabricated with different waiting times for FeC@C NP aggregations. In both cases, a waiting time of 3 h gave the highest PCEs (**Figure. S16** and **S17**). The statistical analyses show that there is a trend of J_{SC} and V_{OC} increasing with the waiting time and reducing when the waiting time is longer than 3 h. This verifies the aforementioned plasmonic effect of the aggregated FeC@C NPs, as the increase in J_{SC} is related to the number of absorbed photons.^{90,91} For the devices with the best performance, the PSCs where FeC@C NPs were coated on FTO gave a PCE of 20.57% with J_{SC} of 25.05 mA cm⁻², V_{OC} of 1.10 V, and FF of 0.74 (**Figure. 4g** and **Table 1**). The PSCs with FeC@C NPs on SnO₂ exhibited an even higher PCE of 21.15% with a J_{SC} of 25.73 mA cm⁻², V_{OC} of 1.11 V, and FF of 0.74 (**Figure. 4h** and **Table 2**). The difference in device performance was mainly due to the J_{SC} values. In general, J_{SC} reflects the photon-to-current conversion efficiency not only by the enhanced intensity of sunlight but also by the perovskite crystal domain size.^{19–21,92–95} The PSCs with FeC@C NPs on FTO exhibited a larger crystal domain size (**Figure. 4c** and **4d**). Nevertheless, PSCs with FeC@C NPs on SnO₂ produced a much higher J_{SC} owing to the FeC@C NPs right under the perovskite film, inducing the plasmonic effect in closer proximity. Steady-state PL and time-resolved (tr-PL) of perovskite films on SnO₂/FeC@C NPs/FTO samples and FeC@C NPs/SnO₂/FTO samples were carried out at

different waiting times. The increase in quenching of the PL spectra of both types of samples over the waiting time as well as the blueshifts indicate that the application of FeC@C NPs enhances the charge transfer and reduces the number of trap sites in SnO₂.⁹⁶ This explains the increase in V_{OC} and FF of the FeC@C NP-applied PSCs in both the cases of FeC@C NPs above/under the SnO₂ layer. We postulate that the high electron affinity of the carbon shell as well as the host–guest electronic interaction^{37–40} augmenting exciton extraction. The higher external quantum efficiency (EQE) of the PSC using FeC@C NPs than that of the control device in the short-wavelength region from 300 nm to 600 nm is suspected to originate from the enhanced electron collection by the FeC@C NPs next to SnO₂.⁹⁷ The higher EQE of the PSC using the FeC@C NPs in the long-wavelength region from 650 nm to 800 nm corresponds to the greater light absorption due to the plasmonic effect (**Figure. S18**). The device stability under constant illumination of one sun was checked to examine ion migration. All unencapsulated FeC@C NP-used PSCs showed good operational stability equal to that of the control device in both cases of FeC@C NPs above/under the SnO₂ layer. This indicates that there is no ion migration occurring within the device system owing to the Fe particles being fully encapsulated by the carbon shell.

3. Conclusion

The synthesis and extraction of FeC@C NPs from aerosol-synthesized CNT films were demonstrated. Assortments of aerosol-synthesized CNTs containing FeC@C NPs of different sizes were dispersed in CB. FeC@C NPs with a desired size were collected through intensive

sonication and filtration. The presence and size of the FeC@C NPs were verified using various techniques such as SEM, EDS, AFM, and TEM. The FeC@C NPs showed aggregation over time, entailing an increasing intensity of the gap-surface plasmon effect. The self-aggregated FeC@C NPs have great potential for application in optoelectronic devices because tailoring the number and position of the NPs in close-packed clusters can induce diverse plasmon modes exhibiting strong magnetic and Fano resonance. Capitalizing on this point, PSCs were fabricated with aggregated NPs placed on the SnO₂ layer and the FTO layer. The addition of the FeC@C NPs to PSCs improved the PCE, which was attributed to both the enhanced light absorption and charge transfer by the plasmonic effect and by the host-guest electronic interaction, respectively. The excellent device stability shown by the FeC@C NP-added PSCs proves that the metal ions in the NPs did not migrate into the perovskite layer even when FeC@C NPs were next to the perovskite film.

4. Experimental Section

Preparation of FeC@C: Aerosol-synthesized CNT films containing a large number of FeC@C NPs were prepared using the floating-catalyst aerosol chemical vapor deposition (CVD) method. Ferrocene (100 cc) was vaporized by passing CO through a cartridge filled with ferrocene powder. To stabilize the synthesis, 1.4% CO₂ was added to CO. The flow containing ferrocene vapor was introduced to the high-temperature zone of a quartz tube reactor through a water-cooled probe and mixed with additional CO. Ferrocene vapor was thermally decomposed in the gas phase of the aerosol CVD reactor at 850 °C. CO gas was supplied at 0.35 L min⁻¹ and decomposed on the Fe NPs, resulting in the growth of FeC@C NPs. The as-synthesized CNTs and FeC@C NPs were collected by passing the flow through CNTs, and FeC@C NPs were collected by filtering the flow through a nitrocellulose membrane filter (Millipore Corp., USA; HAWP, 0.45- μ m pore diameter) downstream of the reactor for 93 h. The FeC@C-containing

film was placed in a vial containing CB. To separate the intertwined FeC@C/CNT, sonication was performed at 40k Hz for 6 h. This process separated the FeC@C particles from the CNTs. The supernatant containing FeC@C NPs was separated by centrifugation at 10,000 rpm for 20 min. The supernatant was filtered using PTFE with a pore diameter of 0.20 μm . The presence and size of the FeC@C NPs were determined using various analytical equipment described in the Results and Discussion section.

Perovskite Precursor: Formamidinium iodide (FAI), methylammonium bromide (MABr), lead(II) iodide (PbI_2 , 99.99%), and lead(II) bromide (PbBr_2 , >98%) were purchased from Tokyo Chemical Industry Co., Ltd. (Tokyo, Japan). Cesium iodide (CsI, 99.998%) and tin(II) oxide (SnO_2 , 15% in H_2O) were purchased from Alfa Aesar Co., Ltd. (Ward Hill, MA, USA). 2,2,7,7-tetrakis(*N,N*-di-*p*-methoxyphenylamine)-9,9-spirobifluorene (spiro-MeOTAD), lithium bis(trifluoromethanesulfonyl)imide (Li-TFSI), tris[2-(1*H*-pyrazol-1-yl)-4-*tert*-butylpyridine]-cobalt(III)-tris[bis-(trifluoromethylsulfonyl)imide] (FK209), 4-*tert*-butylpyridine (*t*BP), isopropyl alcohol (IPA), and chlorobenzene (CB) were purchased from Sigma-Aldrich Co., Ltd. (St. Louis, MO, USA). Dehydrated dimethylsulfoxide (DMSO, super dehydrated) and dimethylformamide (DMF, super dehydrated) were purchased from FUJIFILM Wako Pure Chemical Co., Ltd. (Osaka, Japan).

Preparation of Perovskite Film: A $\text{Cs}_{0.05}\text{FA}_{0.80}\text{MA}_{0.15}\text{PbI}_{2.75}\text{Br}_{0.25}$ -based perovskite precursor solution was prepared by dissolving CsI (44.4 mg, 0.171 mmol), PbI_2 (1432 mg, 3.11 mmol), PbBr_2 (61 mg, 0.166 mmol), FAI (450 mg, 0.64 mmol), and MABr (54.3 mg, 0.16 mmol) in DMF (2400 μL) and DMSO (720 μL). After stirring for 30 min at 45°C, the solution was filtered through a 0.2- μm PTFE filter. The precursor was spin-coated at 3000 rpm for 30 s on the SnO_2 layer. This was followed by the application of 300 μL of CB antisolvent. The annealing process was performed at 150°C for 10 min. The spiro-MeOTAD solution was prepared by mixing

108.45 mg spiro-MeOTAD, 13.65 mg of Li-TFSI, 20.25 mg of FK209, and 43.2 μL of *t*-BP in 1.5 mL of anhydrous chlorobenzene. The hole-transporting layer was deposited from the 80- μL spiro-MeOTAD solution at 3000 rpm for 20 s. Finally, a 100-nm-thick Au anode was fabricated by thermal deposition under a pressure of 10^{-7} Torr.

Fabrication of PSCs: FTO substrates, pre-patterned FTO/glass substrates ($7 \Omega \text{ sq}^{-1}$, $25 \times 25 \text{ mm}^2$) (Asahi glass) were cleaned using the RCA-2 (H_2O_2 - NCl - H_2O) procedure for 15 min. The substrates were further cleaned by sonication with distilled water, acetone, and isopropanol in an ultrasonic bath for 15 min. Subsequently, tin(IV) oxide (SnO_2 , 15% in H_2O colloidal dispersion, Alfa Aesar) solution was prepared by adding 5 mL of ethanol to 0.1128 g at room temperature, followed by sonication for approximately 1 min. The SnO_2 solution was then filtered through a 0.45- μm PTFE filter. Next, the SnO_2 layer was spin-coated on the FTO glass (or SnO_2 layer) at 2000 rpm for 30 s, which was later annealed at 150°C for 30 min. A solution containing FeC@C NPs was drop-casted on either FTO or SnO_2 after a designated waiting time from sonication to induce π - π aggregation. When the FeC@C solvent was dried, 100 μL of the perovskite solution was filtered through a 0.45- μm PTFE filter before being spin-coated on the SnO_2 layer at 7000 rpm for 40 s. Antisolvent (1 mL of diethyl ether) was applied during the spin-coating of the perovskite solution at 37–38 s after spin-coating, followed by annealing at 150°C for 10 min. The spiro-MeOTAD solution was prepared by mixing 90.9 mg spiro-MeOTAD, 23 μL of a stock solution of 516 mg mL^{-1} Li-TFSI in anhydrous acetonitrile, 10 μL of a stock solution of 395 mg mL^{-1} FK209 in anhydrous acetonitrile, and 39 μL of *t*-BP in 1.0 mL of anhydrous chlorobenzene. The hole-transporting layer was deposited from the 100 μL spiro-MeOTAD solution at 4000 rpm for 20 s. Finally, an 80-nm-thick Au anode was fabricated by thermal deposition under a pressure of 10^{-6} Torr.

Device and Film Characterizations: The J - V curves of the PSCs under light were measured using a source meter (Keithley 2400, Tektronix) under simulated sunlight irradiation of 1 sun (AM 1.5G; 100 mW cm^{-2}) using a solar simulator (Oriel® Sol3A™ Class AAA solar simulator, model 94043A). The source meter was calibrated using a standard PV reference cell ($2 \text{ cm} \times 2 \text{ cm}$ monocrystalline silicon solar cell, calibrated at NREL, Colorado, USA). The incident photon-to-current conversion efficiency also known as external quantum efficiency (EQE) spectrum was measured using an Oriel® IQE-200™ equipped with a 250-W quartz tungsten halogen lamp as the light source and a monochromator, an optical chopper, a lock-in amplifier, and a calibrated silicon photodetector. Prior to the use of light, the spectral response and light intensity were calibrated using a monosilicon detector. The impedance response was measured over the range of 1 Hz to 1 MHz with an oscillation amplitude of 15 mV under dark conditions (Bio-Logic VMP-3). The experimental data were simulated using commercial Z-view software to estimate the values of each component using the corresponding equivalent circuits. The film surface and cross-sectional morphology were characterized via field emission scanning electron microscopy (FE-SEM, HITACHI Regulus8100). Photoluminescence (PL) was measured using a Quantaurus-QY plus (C-13534-12) from Hamamatsu Co., Ltd.

Computational Analysis: The finite-difference time-domain (FDTD) simulation of the plasmonic scattering and absorption of NPs was performed using the Lumerical FDTD software. The model comprised a 3D spatial domain of $80 \times 80 \times 80 \text{ nm}^3$, which was meshed into 0.1 nm in all xyz coordinates, and its boundary condition was set as a perfectly matched layer that absorbs all outgoing waves. An optical source with a wavelength ranging from 300 nm to 800 nm generates a plane wave propagating toward a target set of scatterers designated with a specific number of NPs with a core diameter (D) and shell thickness (t). The source type was chosen as a total-field scattered-field, where the model considers only the scattered portion of optical energy from NPs and ignores the rest of the portion that does not interact with any

objects. Two detectors (frequency-domain field and power) surrounded the simulation domain and monitored the absorbed and scattered optical energy by the NPs, resulting in effective scattering/absorption cross-sections. The optical field pattern within the NPs aligned in a plane normal to the incoming plane wave was recorded using a DFT monitor. The time-domain simulation was terminated by either a 100-fs time limit or an early shutoff of 10^{-5} .

Supporting Information

Supporting Information is available from the Wiley Online Library or from the author.

Acknowledgements

+: J.H and K.K contributed equally to this work. This work was supported by the National Research Foundation of Korea (NRF) funded by the Ministry of Science and ICT (MSIT) of the Korean government (NRF-2021R1C1C1009200, NRF-2022R1H1A1A01065316). This research was supported by Sungkyunkwan University (SKKU) and the BK21 FOUR (Graduate School Innovation) funded by the Ministry of Education (MOE, Korea) and NRF. This work was supported by the Academy of Finland (ANCED project). We thank Kyungshin Holdings co. ltd. for financial support.

Conflict of Interest

The authors declare no conflict of interest.

Received: ((will be filled in by the editorial staff))

Revised: ((will be filled in by the editorial staff))

Published online: ((will be filled in by the editorial staff))

References

1. Kim HS, Grätzel M, Park NG, et al. Lead Iodide Perovskite Sensitized All-Solid-State Submicron Thin Film Mesoscopic Solar Cell with Efficiency Exceeding 9%, *Sci. Rep.* 2012; 2:591.
2. Kojima A, Teshima K, Shirai Y, Miyasaka T. Organometal Halide Perovskites as Visible-Light Sensitizers for Photovoltaic Cells, *J. Am. Chem. Soc.* 2009; 131:6050–6051.
3. Park NG, Grätzel M, Miyasaka T, Zhu K, Emery K. Towards stable and commercially available perovskite solar cells, *Nat. Energy.* 2016; 1:16152.
4. Lee MM, Teuscher J, Miyasaka T, Murakami TN, Snaith HJ. Efficient Hybrid Solar Cells Based on Meso-Superstructured Organometal Halide Perovskites, *Science* 2012; 338:643–647.

5. Jeong M, Kim DS, Yang C, et al. Stable perovskite solar cells with efficiency exceeding 24.8% and 0.3-V voltage loss, *Science* 2020; 369:1615–1620.
6. Jeong J, Grätzel M, Kim JY, et al. Pseudo-halide anion engineering for α -FAPbI₃ perovskite solar cells, *Nature*. 2021; 592:381–385.
7. Min H, Kim M, Seok SI, et al. Efficient, stable solar cells by using inherent bandgap of α -phase formamidinium lead iodide, *Science* 2019; 366:749–753.
8. Kim M, Kim GH, Kim DS, et al. Methylammonium Chloride Induces Intermediate Phase Stabilization for Efficient Perovskite Solar Cells, *Joule*. 2019; 3:2179–2192.
9. Sutton RJ, Moore DT, Snaith HJ, et al. Bandgap-Tunable Cesium Lead Halide Perovskites with High Thermal Stability for Efficient Solar Cells, *Adv. Energy Mater.* 2016; 6 :1502458.
10. Eperon GE, Stranks SD, Menelaou C, Johnston MB, Herz LM, Snaith HJ. Formamidinium lead trihalide: a broadly tunable perovskite for efficient planar heterojunction solar cells, *Energy Environ. Sci.* 2014; 7:982.
11. Leijtens T, Bush KA, Prasanna R, McGehee MD. Opportunities and challenges for tandem solar cells using metal halide perovskite semiconductors, *Nat. Energy*. 2018; 3:828–838.
12. Wolf SD, Yum JH, Ballif C, et al. Organometallic halide perovskites: Sharp optical absorption edge and its relation to photovoltaic performance, *J. Phys. Chem. Lett.* 2014; 5:1035–1039.
13. Jena AK, Kulkarni A, Miyasaka T. Halide Perovskite Photovoltaics: Background, Status, and Future Prospects, *Chem. Rev.* 2019; 119:3036–3103.
14. Bi D, Yi C, Grätzel M, et al. Polymer-templated nucleation and crystal growth of perovskite films for solar cells with efficiency greater than 21%, *Nat. Energy*. 2016; 1:16142.
15. Han TH, Lee JW, Yang Y, et al. Perovskite-polymer composite cross-linker approach for highly-stable and efficient perovskite solar cells, *Nat. Commun.* 2019;10:520.
16. Lee JW., Bae SH, Yang Y, et al. A Bifunctional Lewis Base Additive for Microscopic Homogeneity in Perovskite Solar Cells, *Chem.* 2017; 3:290–302.

17. Guo Y, Sato W, Nakamura E. Citric Acid Modulated Growth of Oriented Lead Perovskite Crystals for Efficient Solar Cells, *J. Am. Chem. Soc.* 2017; 139:9598–9604.
18. Liang PW, Chueh CC, Williams ST, Jen AKY. Roles of Fullerene-Based Interlayers in Enhancing the Performance of Organometal Perovskite Thin-Film Solar Cells, *Adv. Energy Mater.* 2015; 5:1402321.
19. Lin HS, Matsuo Y, Maruyama S, et al. Polyaromatic Nanotweezers on Semiconducting Carbon Nanotubes for the Growth and Interfacing of Lead Halide Perovskite Crystal Grains in Solar Cells, *Chem. Mater.* 2020; 32:5125–5133.
20. Seo S, Jeon I, Maruyama S, et al. Semiconducting carbon nanotubes as crystal growth templates and grain bridges in perovskite solar cells, *J. Mater. Chem. A.* 2019; 7:12987–12992.
21. Lin HS, Matsuo Y, Oh JW, et al. Denatured M13 Bacteriophage-Templated Perovskite Solar Cells Exhibiting High Efficiency, *Adv. Sci.* 2020; 7:2000782.
22. Liu S, Guan Y, Han H, et al. A Review on Additives for Halide Perovskite Solar Cells, *Adv. Energy Mater.* 2020; 10:1902492.
23. Kim KS, Han JY, Maruyama S, Balaban M, Jeon I. Role and Contribution of Polymeric Additives in Perovskite Solar Cells: Crystal Growth Templates and Grain Boundary Passivators, *Sol. RRL.* 2021; 2000783.
24. Zhang F, Zhu K. Additive Engineering for Efficient and Stable Perovskite Solar Cells, *Adv. Energy Mater.* 2020; 10:1902579.
25. Hartland GV. Optical Studies of Dynamics in Noble Metal Nanostructures, *Chem. Rev.* 2011; 111:3858–3887.
26. Silvera Batista CA, Larson RG, Kotov NA. Nonadditivity of nanoparticle interactions, *Science* 2015; 350:1242477.
27. Murphy CJ. MATERIALS SCIENCE: Nanocubes and Nanoboxes, *Science* 2002; 298:2139–2141.
28. Plane JMC. Cosmic dust in the earth's atmosphere, *Chem. Soc. Rev.* 2012; 41:6507.

29. Kiss LB, Söderlund J, Niklasson GA, Granqvist CG. New approach to the origin of lognormal size distributions of nanoparticles, *Nanotechnology*. 1999; 10:25–28.
30. Bárcena C, Sra AK, Gao J. Applications of Magnetic Nanoparticles in Biomedicine, in: *Nanoscale Magn. Mater. Appl.* 2009; 591–626.
31. Lu J, Chen Z, Pan F, Curtiss LA, Amine K. The role of nanotechnology in the development of battery materials for electric vehicles, *Nat. Nanotechnol.* 2010; 11.
32. Brongersma ML, Halas NJ, Nordlander P. Plasmon-induced hot carrier science and technology, *Nat. Nanotechnol.* 2015; 10:25–34.
33. Yao K, Zhong H, Jen AKY, et al. Plasmonic Metal Nanoparticles with Core–Shell Structure for High-Performance Organic and Perovskite Solar Cells, *ACS Nano*. 2019; 13:5397–5409.
34. Higgins M, Nam S, Quevedo-Lopez M, Enhanced reproducibility of planar perovskite solar cells by fullerene doping with silver nanoparticles, *J. Appl. Phys.* 2018; 124:065306.
35. Lee HB, Kim WG, Kang JW, et al. Gap Plasmon of Virus-Templated Biohybrid Nanostructures Uplifting the Performance of Organic Optoelectronic Devices, *Adv. Opt. Mater.* 2020; 8:1902080.
36. Singh A, Dey A, Das D, Iyer PK. Combined influence of plasmonic metal nanoparticles and dual cathode buffer layers for highly efficient rrP3HT:PCBM-based bulk heterojunction solar cells, *J. Mater. Chem. C*. 2017; 5:6578–6587.
37. Xiao M, Zhu J, Feng L, Liu C, Xing W. Meso/Macroporous Nitrogen-Doped Carbon Architectures with Iron Carbide Encapsulated in Graphitic Layers as an Efficient and Robust Catalyst for the Oxygen Reduction Reaction in Both Acidic and Alkaline Solutions, *Adv. Mater.* 2015; 27:2521–2527.
38. Yao K, Huang H, Jen AKY, et al. Fullerene-Anchored Core-Shell ZnO Nanoparticles for Efficient and Stable Dual-Sensitized Perovskite Solar Cells, *Joule*. 2019; 3:417–431.

39. Cai C, Zhang J, Zhu Y, et al. Enhanced hole extraction by NiO nanoparticles in carbon-based perovskite solar cells, *Electrochim. Acta*. 2019; 312:100–108.
40. Yao K, Huang H, Jen AKY, et al. A copper-doped nickel oxide bilayer for enhancing efficiency and stability of hysteresis-free inverted mesoporous perovskite solar cells, *Nano Energy*. 2017; 40:155–162.
41. Barnes WL, Dereux A, Ebbesen TW. Surface plasmon subwavelength optics, *Nature*. 2003; 424:824–830.
42. Alloyeau D, Mottet C, Ricolleau C, eds. *Nanoalloys*, London:Springer London, 2012.
43. Lee JM, Lim J, Kim SO. Synergistic Concurrent Enhancement of Charge Generation, Dissociation, and Transport in Organic Solar Cells with Plasmonic Metal-Carbon Nanotube Hybrids, *Adv. Mater.* 2015; 27:1519–1525.
44. Kang MG, Xu T, Park HJ, Luo X, Guo LJ. Efficiency Enhancement of Organic Solar Cells Using Transparent Plasmonic Ag Nanowire Electrodes, *Adv. Mater.* 2010; 22:4378–4383.
45. Stratakis E, Kymakis E. Nanoparticle-based plasmonic organic photovoltaic devices, *Mater. Today*. 2013; 16:133–146.
46. Lee YH, Li LJ, Lin TW, et al. Synthesis of large-area MoS₂ atomic layers with chemical vapor deposition, *Adv Mater.* 2012; 24:2320–2325.
47. Yuan Z, Jin Y, Sun B, et al. Hot-Electron Injection in a Sandwiched TiO_x-Au-TiO_x Structure for High-Performance Planar Perovskite Solar Cells, *Adv. Energy Mater.* 2015; 5:1500038.
48. Kim GM, Tatsuma T. Semi-transparent Perovskite Solar Cells Developed by Considering Human Luminosity Function, *Sci. Rep.* 2017; 7:10699.
49. Carretero-Palacios S, Calvo ME, Míguez H. Absorption Enhancement in Organic–Inorganic Halide Perovskite Films with Embedded Plasmonic Gold Nanoparticles, *J. Phys. Chem. C*. 2015; 119:18635–18640.

50. Carretero-Palacios S, Jiménez-Solano A, Míguez H. Plasmonic Nanoparticles as Light-Harvesting Enhancers in Perovskite Solar Cells: A User's Guide, *ACS Energy Lett.* 2016; 1:323–331.
51. Domanski K, Hagfeldt A, Grätzel M, et al. Not All That Glitters Is Gold: Metal-Migration-Induced Degradation in Perovskite Solar Cells, *ACS Nano.* 2016; 10:6306–6314.
52. Jeon I, Maruyama S, Matsuo Y, et al. Controlled Redox of Lithium-Ion Endohedral Fullerene for Efficient and Stable Metal Electrode-Free Perovskite Solar Cells, *J. Am. Chem. Soc.* 2019; 141:16553–16558.
53. Chen J, Lee D, Park NG. Stabilizing the Ag Electrode and Reducing J – V Hysteresis through Suppression of Iodide Migration in Perovskite Solar Cells, *ACS Appl. Mater. Interfaces.* 2017; 9:36338–36349.
54. Chen H, Yang S. Carbon-Based Perovskite Solar Cells without Hole Transport Materials: The Front Runner to the Market?, *Adv. Mater.* 2017; 1603994.
55. Kurotobi K, Murata Y. A Single Molecule of Water Encapsulated in Fullerene C60, *Science* 2011; 333:613–616.
56. Heath JR, Tittel FK, Smalley RE, et al. Lanthanum complexes of spheroidal carbon shells, *J. Am. Chem. Soc.* 1985; 107:7779–7780.
57. Tellgmann R, Krawez N, Lin SH, Hertel IV. Campbell EEB, Endohedral fullerene production, *Nature.* 1996; 382:407–408.
58. Aoyagi S, Nishibori E, Tobita H, et al. A layered ionic crystal of polar Li@C60 superatoms, *Nat. Chem.* 2010; 2:678–683.
59. Luo N, Li X, Wang X, Yan H, Zhang C, Wang H. Synthesis and characterization of carbon-encapsulated iron/iron carbide nanoparticles by a detonation method, *Carbon N. Y.* 2010; 48:3858–3863.
60. Khurshid H, Abdu YA, Devlin E, Issa BA, Hadjipanayis GC. Chemically synthesized nanoparticles of iron and iron-carbides, *RSC Adv.* 2020; 10:28958–28964.

61. Yu S, Chow GM. Synthesis, structural, magnetic, and cytotoxic properties of iron oxide coated iron/iron-carbide nanocomposite particles, *J. Appl. Phys.* 2005; 98:114306.
62. Davydov V, Rakhmanina A, Khabashesku V, et al. Solid state synthesis of carbon-encapsulated iron carbide nanoparticles and their interaction with living cells, *J. Mater. Chem. B.* 2014; 2:4250–4261.
63. Khurshid H, Tzitzios V, Li W, Hadjipanayis CG. Size and composition control of core-shell structured iron/iron-oxide nanoparticles, *J. Appl. Phys.* 2010; 107:09A333.
64. Kim JH, Kim J, Shon Y, et al. Synthesis of carbon-encapsulated iron carbide nanoparticles on a polyimide thin film, *Nanotechnology.* 2007; 18:115609.
65. Nasibulin AG, Kaskela A, Kauppinen EI, et al. Multifunctional Free-Standing Single-Walled Carbon Nanotube Films, *ACS Nano.* 2011; 5:3214–3221.
66. Wirth CT, Robertson J, Hofmann S, et al. The Phase of Iron Catalyst Nanoparticles during Carbon Nanotube Growth, *Chem. Mater.* 2012; 24:4633–4640.
67. McLean B, Kauppinen EI, Page AJ. Initial competing chemical pathways during floating catalyst chemical vapor deposition carbon nanotube growth, *J. Appl. Phys.* 2021; 129:044302.
68. Li GC, Zhang Q, Maier SA, Lei D. Plasmonic particle-on-film nanocavities: a versatile platform for plasmon-enhanced spectroscopy and photochemistry, *Nanophotonics.* 2018; 7:1865–1889.
69. Lyu S, Wang L, Wang Y, et al. Stabilization of ϵ -iron carbide as high-temperature catalyst under realistic Fischer–Tropsch synthesis conditions, *Nat. Commun.* 2020; 11:6219.
70. Lee HK, Jung H, Park JC, et al. Extremely productive iron-carbide nanoparticles on graphene flakes for CO hydrogenation reactions under harsh conditions, *J. Catal.* 2019; 378:289–297.
71. Cao CY, Wu ZY, Song WG, et al. Low-Cost Synthesis of Flowerlike α -Fe₂O₃ Nanostructures for Heavy Metal Ion Removal: Adsorption Property and Mechanism, *Langmuir.* 2012; 28:4573–4579.

72. Cuenca JA, Bugler K, Porch A, et al. Study of the magnetite to maghemite transition using microwave permittivity and permeability measurements, *J. Phys. Condens. Matter.* 2016; 28:106002.
73. Amendola V, Riello P, Meneghetti M. Magnetic Nanoparticles of Iron Carbide, Iron Oxide, Iron@Iron Oxide, and Metal Iron Synthesized by Laser Ablation in Organic Solvents, *J. Phys. Chem. C.* 2011; 115:5140–5146.
74. Wang X, Zhu K, Hou Y, et al. Iron carbides: Magic materials with magnetic and catalytic properties, *J. Magn. Magn. Mater.* 2019; 489:165432.
75. Sajitha EP, Sarkar S, Bansal C, et al. Size-dependent magnetic properties of iron carbide nanoparticles embedded in a carbon matrix, *J. Phys. Condens. Matter.* 2007; 19:046214.
76. Bryant
77. Notarianni M, Vernon K, Motta N, et al. Plasmonic effect of gold nanoparticles in organic solar cells, *Sol. Energy.* 2014; 106:23–37.
78. Wang L, Hasanzadeh Kafshgari M, Meunier M. Optical Properties and Applications of Plasmonic-Metal Nanoparticles, *Adv. Funct. Mater.* 2020; 30:2005400.
79. Chen AL, Jackson MA, Drezek RA, et al. Change in Optical Properties of Plasmonic Nanoparticles in Cellular Environments are Modulated by Nanoparticle PEGylation and Serum Conditions, *Nanoscale Res. Lett.* 2016; 11:1–12.
80. Ni ZH, Wang HM, Shen ZX, et al. Graphene Thickness Determination Using Reflection and Contrast Spectroscopy, *Nano Lett.* 2007; 7:2758–2763.
81. Ye S, Huang H, Wang G, et al. Thickness-Dependent Strain Effect on the Deformation of the Graphene-Encapsulated Au Nanoparticles, *J. Nanomater.* 2014; 2014:1–6.
82. Li W. Physics Models of Plasmonics: Single Nanoparticle, Complex Single Nanoparticle, Nanodimer, and Single Nanoparticle over Metallic Thin Film, *Plasmonics.* 2018; 13:997–1014.
83. Lee JW, Jeon I, Yang Y, et al. Vapor-Assisted Ex-Situ Doping of Carbon Nanotube toward Efficient and Stable Perovskite Solar Cells, *Nano Lett.* 2019; 19:2223–2230.

84. Thote A, Jeon I, Matsuo Y, et al. Stable and Reproducible 2D/3D Formamidinium–Lead–Iodide Perovskite Solar Cells, *ACS Appl. Energy Mater.* 2019; 2:2486–2493.
85. Peña-Álvarez M, Del Corro E, Langa F, Baonza VG, Taravillo M. Morphological changes in carbon nanohorns under stress: a combined Raman spectroscopy and TEM study, *RSC Adv.* 2016; 6:49543–49550.
86. Ye J, Hutchison JA, Van Dorpe P, et al. Excitation wavelength dependent surface enhanced Raman scattering of 4-aminothiophenol on gold nanorings, *Nanoscale.* 2012; 4:1606.
87. Kumar S, Kumar P, Das A, Pathak CS. Surface-Enhanced Raman Scattering: Introduction and Applications, *Recent Advances in Nanophotonics.* 2020; 1:1–24.
88. Jeon TY, Kim DJ, Kim DH, et al. Nanostructured plasmonic substrates for use as SERS sensors, *Nano Converg.* 2016; 3:1–20
89. Hammond JL, Bhalla N, Rafiee SD, Estrela P. Localized Surface Plasmon Resonance as a Biosensing Platform for Developing Countries, *Biosensors.* 2014; 4:172–188.
90. V.L. Dalal, A. Rothwarf. Comment on "A simple measurement of absolute solar cell efficiency", *J. Appl. Phys.* 50 (1979) 2980–2981.
91. Liu T, Yan H, Tang B, et al. Concurrent improvement in J_{SC} and V_{OC} in high-efficiency ternary organic solar cells enabled by a red-absorbing small-molecule acceptor with a high LUMO level, *Energy Environ. Sci.* 2020; 13:2115–2123.
92. Han JY, Kim KS, Jeon I, et al. Genetic Manipulation of M13 Bacteriophage for Enhancing the Efficiency of Virus-Inoculated Perovskite Solar Cells with a Certified Efficiency of 22.3%, *Adv. Energy Mater.* 2021; 2101221.
93. Eperon GE, Stranks SD, Snaith HJ, et al. Formamidinium lead trihalide: a broadly tunable perovskite for efficient planar heterojunction solar cells, *Energy Environ. Sci.* 2014; 7:982.
94. Jeon NJ, Noh JH, Seok SI, et al. Solvent engineering for high-performance inorganic–organic hybrid perovskite solar cells, *Nat. Mater.* 2014; 13:897–903.

95. Tidhar Y, Rybtchinski B, Kirmayer S, et al. Crystallization of Methyl Ammonium Lead Halide Perovskites: Implications for Photovoltaic Applications, *J. Am. Chem. Soc.* 2014; 136:13249–13256.
96. Kondo Y, Yanai M, Hatakeyama T, et al. Narrowband deep-blue organic light-emitting diode featuring an organoboron-based emitter, *Nat. Photonics.* 2019; 13:678–682.
97. Li J, Cushing SK, Wu N, et al. Plasmon-induced resonance energy transfer for solar energy conversion, *Nat. Photonics.* 2015; 9:601–607.

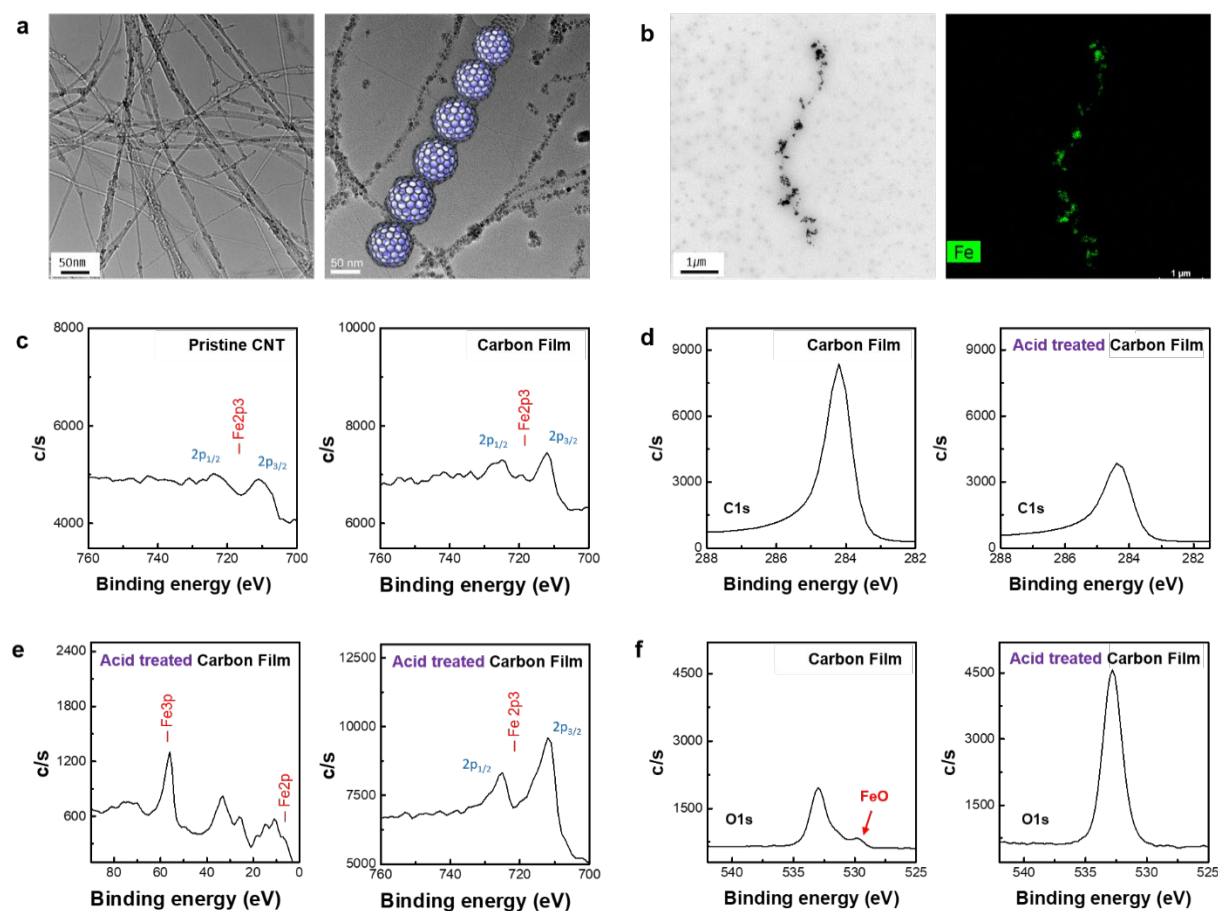


Figure 1. (a) TEM image of the aerosol-synthesised carbon film. (b) Result of EDS analysis through TEM to confirm the existence of Fe components. (c) XPS result of iron region (Fe_{2p₃}) in pristine CNT and carbon film. (c-f) XPS result of the C_{1s} peak, iron region (Fe_{3p}, Fe_{2p}) and O_{1s} peak before and after acid treatment on the carbon film.

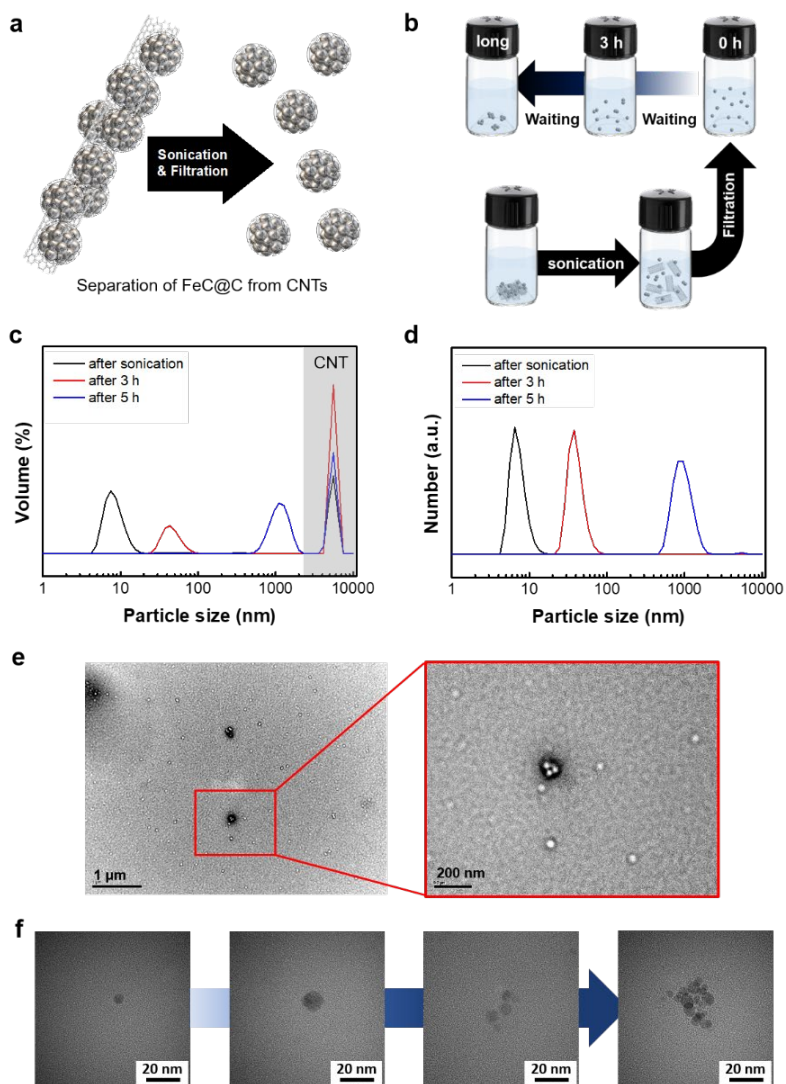


Figure 2. (a–b) Illustration of a method of separating FeC@C NPs from CNT. (c–d) DLS analysis of depending on the waiting time. (e) FeC@C NPs and enlarged TEM images. (f) HR-TEM results of FeC@C NPs that are aggregated depending on the waiting time.

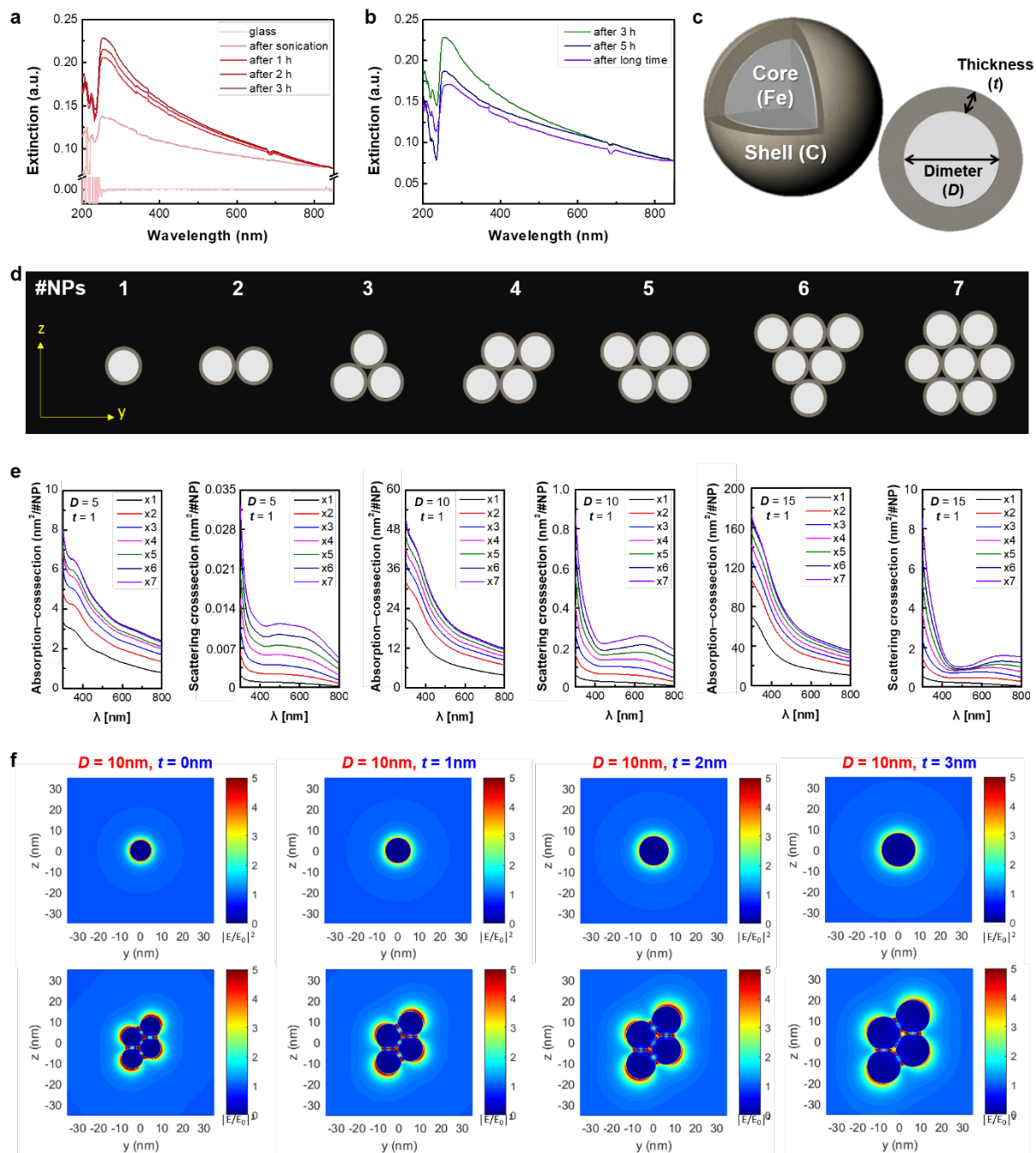


Figure 3. Optical analysis of FeC@C NPs (a-b) UV–Vis results of FeC@C NPs by waiting time, (c) Schematic illustration of FeC@C NPs, (d) geometry by number of FeC@C NPs, (e) When the t is 1 nm, graphs of absorption cross-section and scattering cross-section according to the change in the D , (f) When the D is 10 nm, the electric field according to the change in the t .

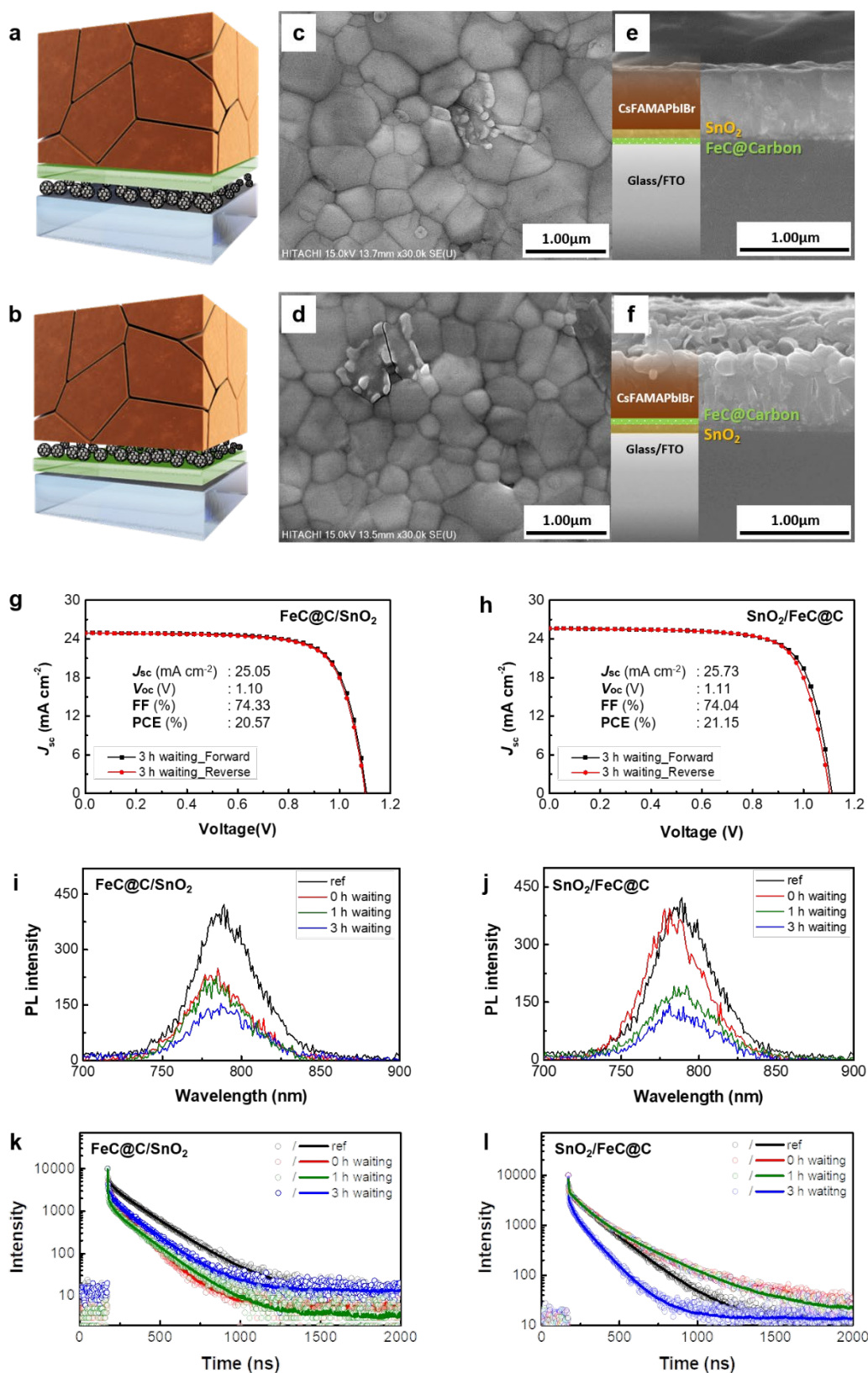


Figure 4. (a–b) Configurational structure and (c–f) SEM image of two type devices. (g–h) J - V curves of optimized devices based on the photovoltaic performance and the location of FeC@C NPs. (i–l) Steady-state PL and tr-PL of perovskite films on SnO₂/FeC@C NPs/FTO samples and FeC@C NPs/SnO₂/FTO samples under different waiting times.

Table 1. Photovoltaic parameters of the PSCs with SnO₂ on FeC@C NPs under one sun (AM 1.5 G, 100 mW cm⁻²).

Device structure and NP aggregation time		J_{sc} (mA cm ⁻²)	V_{oc} (V)	FF (%)	PCE (%)	R_s (Ω ·cm ²)	R_{sh} (Ω ·cm ²)
Au	ref	24.64 [24.77]	1.10 [1.10]	72.89 [70.77]	19.71 [19.35]	39.34	57089.70
Spiro-MeOTAD							
Perovskite	0 h	23.80 [23.73]	1.14 [1.10]	71.32 [70.15]	19.42 [18.23]	37.38	37274.96
SnO ₂	1 h	24.03 [23.69]	1.11 [1.11]	72.70 [72.37]	19.44 [19.09]	43.46	45399.00
FeC@C NPs							
FTO	3 h	25.05 [24.61]	1.10 [1.10]	74.33 [73.00]	20.57 [19.66]	33.81	27866.66
Glass	long	24.62 [23.87]	1.12 [1.10]	74.79 [72.64]	20.55 [19.08]	20.55	31.38

Table 2. Photovoltaic parameters of the PSCs with FeC@C NPs on SnO₂ under one sun (AM 1.5 G, 100 mW cm⁻²).

Device structure and NP aggregation time		J_{sc} (mA cm ⁻²)	V_{oc} (V)	FF (%)	PCE (%)	R_s (Ω ·cm ²)	R_{sh} (Ω ·cm ²)
Au	ref	24.64 [24.77]	1.10 [1.10]	72.89 [70.77]	19.71 [19.35]	39.34	57089.70
Spiro-MeOTAD							
Perovskite	0 h	24.59 [24.08]	1.10 [1.09]	72.17 [70.15]	19.59 [18.46]	38.30	30770.20
FeC@C NPs	1 h	25.07 [24.45]	1.14 [1.15]	69.94 [69.20]	19.91 [19.37]	50.81	47750.96
SnO ₂							
FTO	3 h	25.73 [25.70]	1.11 [1.11]	74.04 [73.44]	21.15 [20.78]	34.13	23741.22
Glass	long	24.19 [23.89]	1.07 [1.08]	76.20 [73.06]	19.78 [18.97]	30.17	20324.67

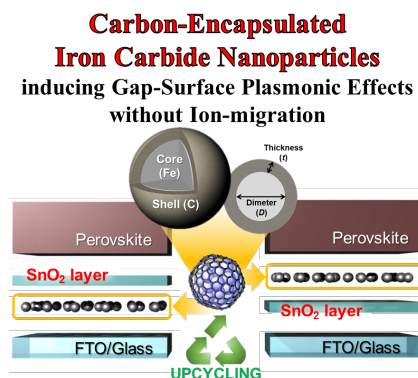
Carbon-encapsulated iron carbide nanoparticles are upcycled from carbon nanotubes for perovskite solar cell application. The nanoparticles aggregate owing to the π - π interaction of the graphitic shells. A gap-surface plasmon effect is induced depending on the degree of the aggregation and arrangements. When applied to solar cells, the efficiency increases from 19.7% to 21.2%. The added nanoparticles do not instigate ion migration as they are encapsulated by the carbon shells.

Keywords

iron nanoparticles, carbon nanoparticles, carbon encapsulation, carbon nanotubes, perovskite solar cells, plasmonic effect

Jiye Han, Kyusun Kim, Mohammad Tavakkoli, Jongmin Lee, Dawoon Kim, In Chung, Aram Lee, Keonwoo Park, Yongping Liao, Jin-Wook Lee, Seung-Ki Lee, Hyokyung Sung*, Esko Kauppinen*, Il Jeon*

Upcycled Synthesis and Extraction of Carbon-Encapsulated Iron Carbide Nanoparticles for Gap Plasmon Applications in Perovskite Solar Cells



(Supporting Information can be included here using this template)

Supporting Information

Upcycled Synthesis and Extraction of Carbon-Encapsulated Iron Carbide Nanoparticles for Gap Plasmon Applications in Perovskite Solar Cells

Jiye Han, Kyusun Kim, Mohammad Tavakkoli, Jongmin Lee, Dawoon Kim, In Chung, Aram Lee, Keonwoo Park, Yongping Liao, Jin-Wook Lee, Seung-Ki Lee, Hyokyung Sung*, Esko Kauppinen*, Il Jeon*

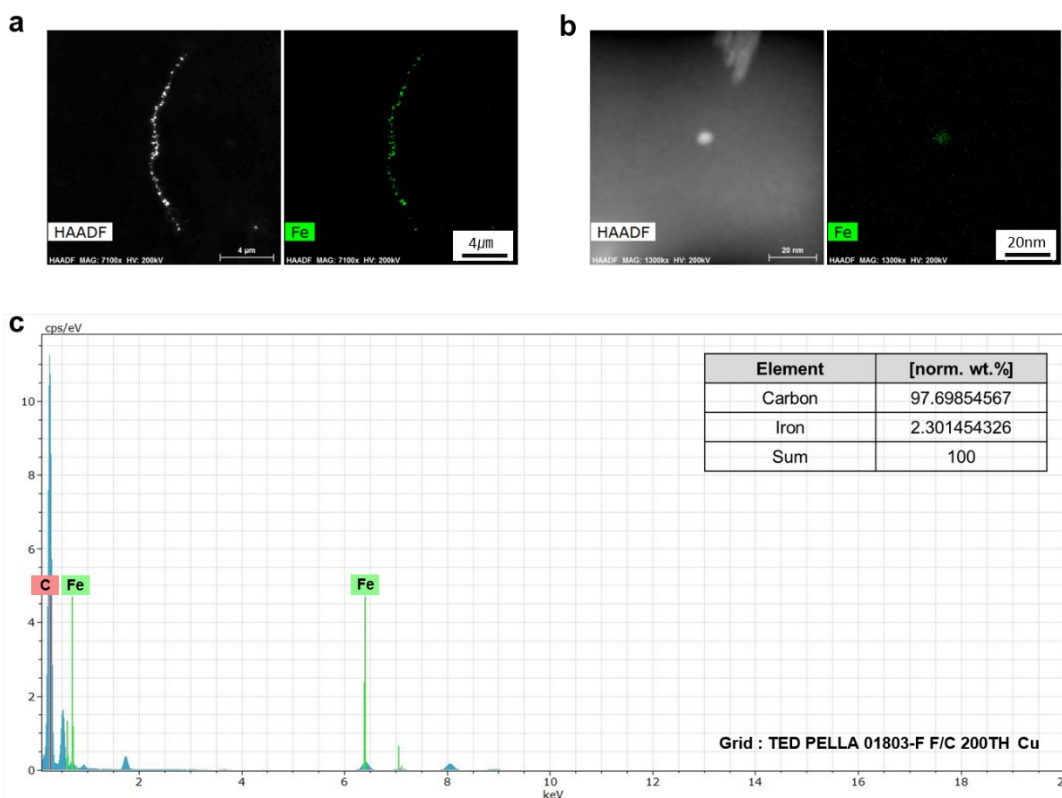


Figure S1. TEM images of a) FeC@C NP along the CNT strand, b) FeC@C NP, and c) EDS graph.

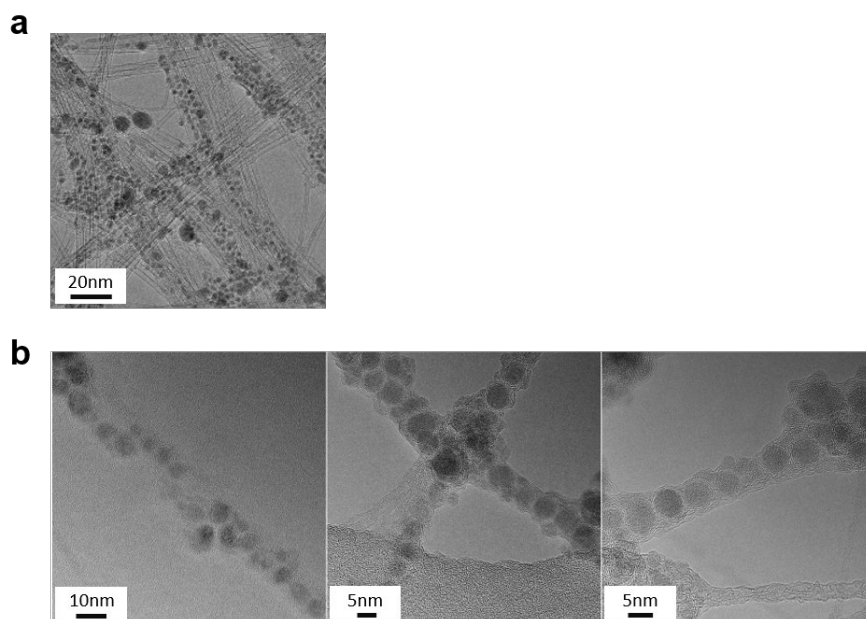


Figure S2. HR-TEM images of the carbon film with a scale bar of a) 20 nm and b) 10 nm and 5 nm.

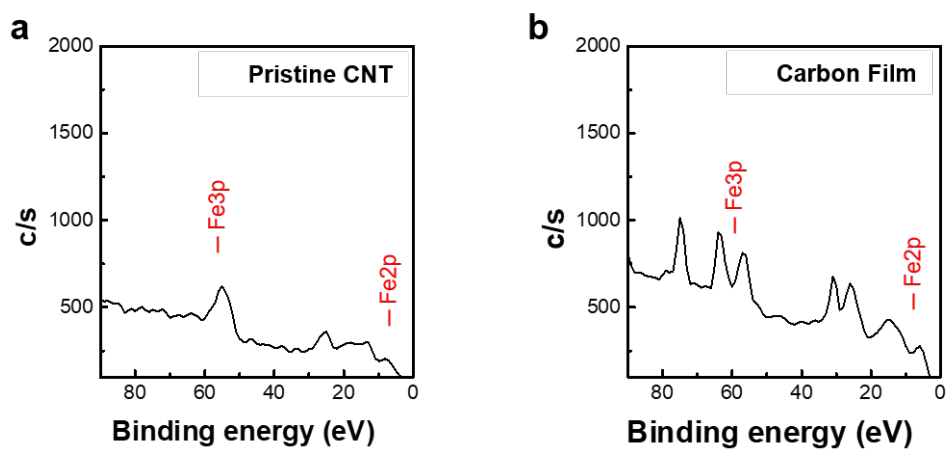


Figure S3. XPS results of Fe peak from pristine CNT and carbon film.



Figure S4. Photographic images of the FeC@C NPs-containing carbon film and the centrifuged solution followed by sonication.



Figure S5. Captured images of the video clip attached as separate supporting information revealing the presence of FeC@C NPs in the obtained solution.

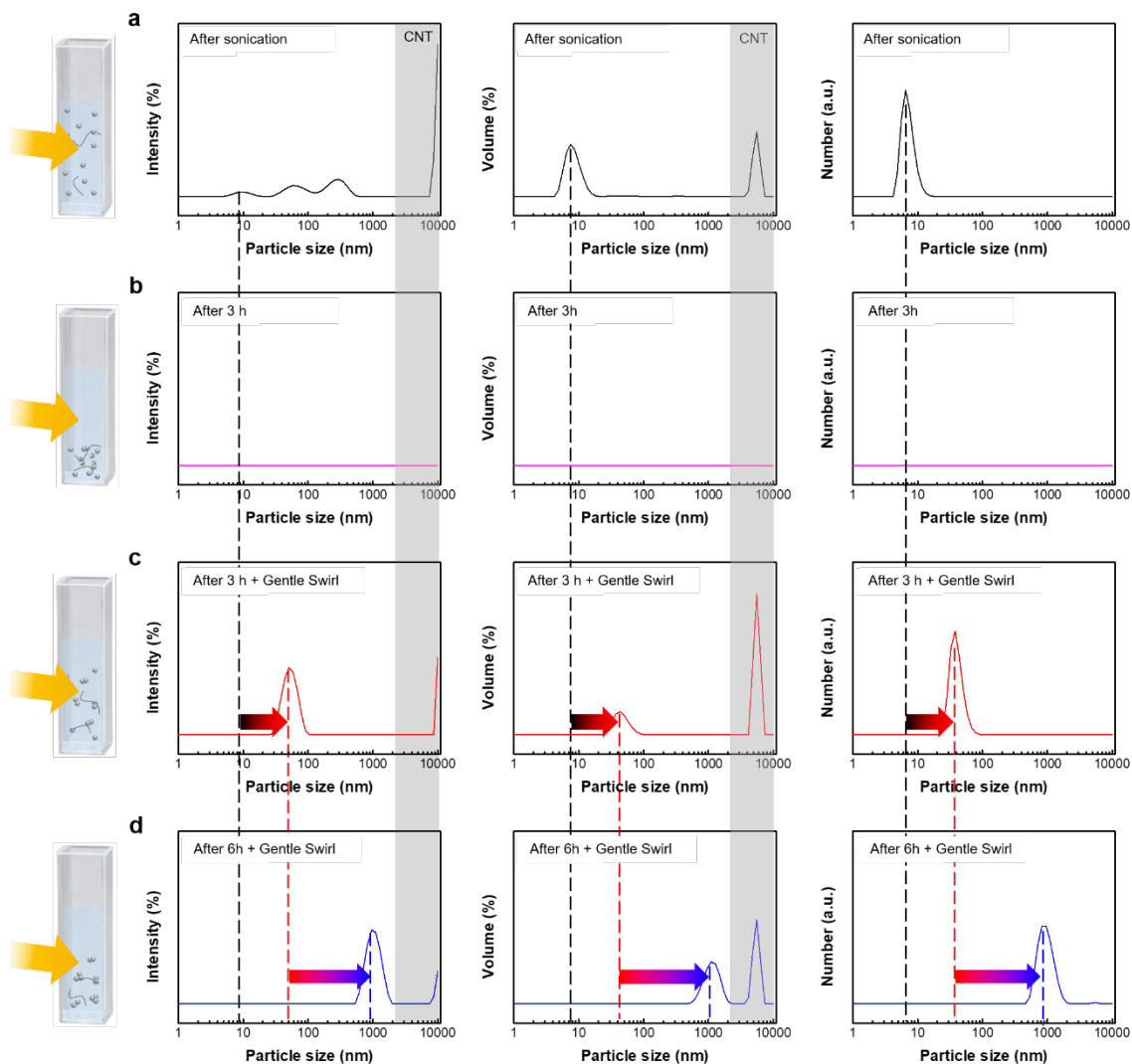


Figure S6. DLS results showing a change in size distribution of FeC@C NPs over time: a) after sonication; b) 3 h after sonication; c) 3 h after sonication + gentle swirl; d) 6 h after sonication + gentle swirl.

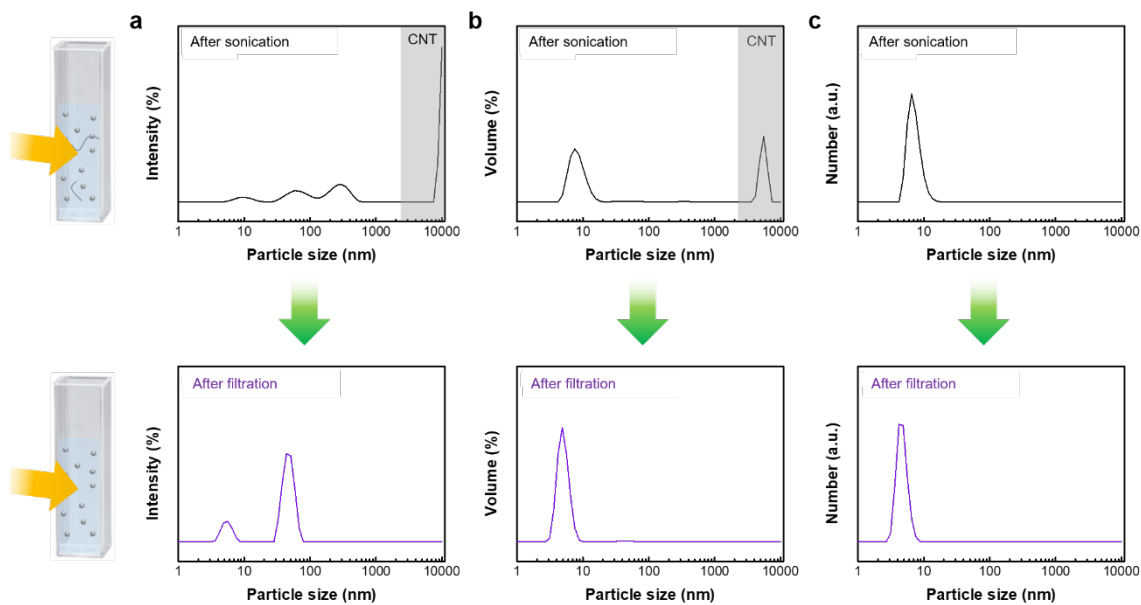


Figure S7. DLS results before and after the filtration: a) intensity, b) volume, and c) number graph.

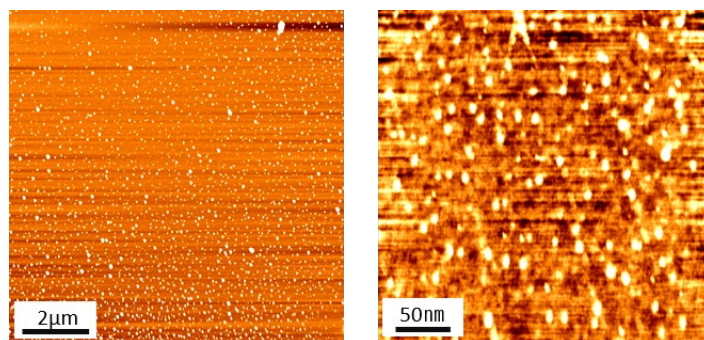


Figure S8. AFM images of FeC@C NPs on a glass substrate.

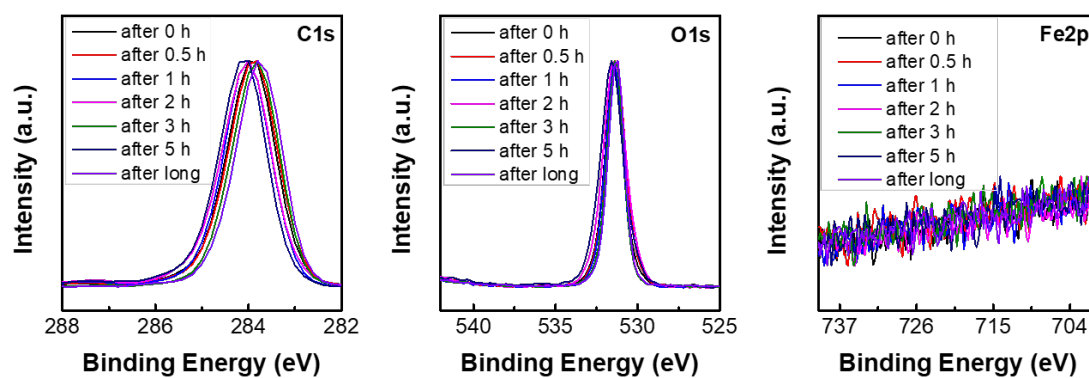


Figure S9. XPS results of C, O, and Fe depending on the waiting time

Table S1. Actual graphene thickness according to the stacked-layer and graphene thickness set in the experiment.

Graphene layer	Actual Thickness (nm)	Effective Thickness (nm)
1 layer	0.335	0
2 layer	0.81	1
3 layer	1.285	1
4 layer	1.76	2
7 layer	3.185	3

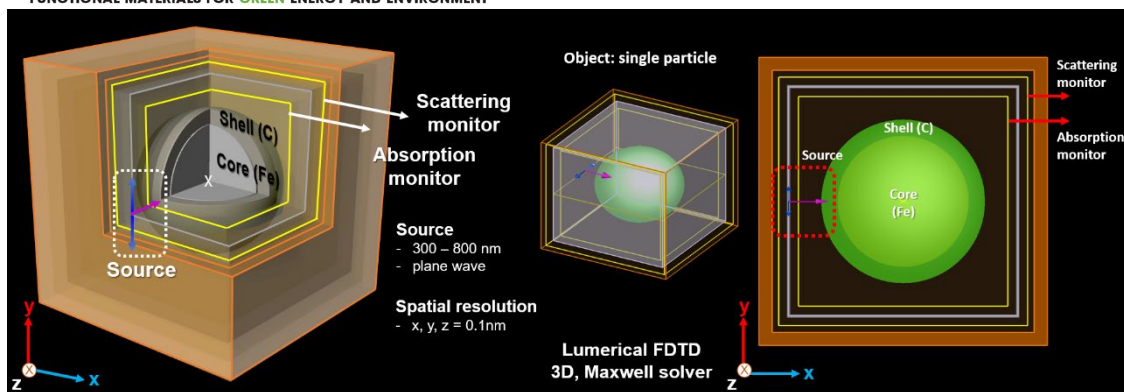
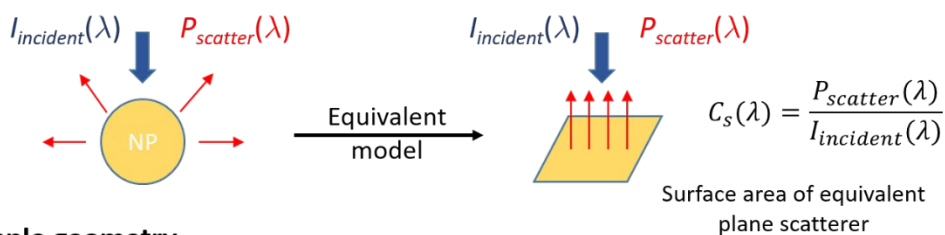


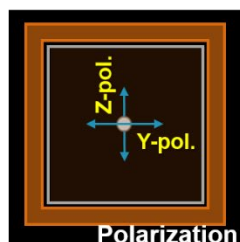
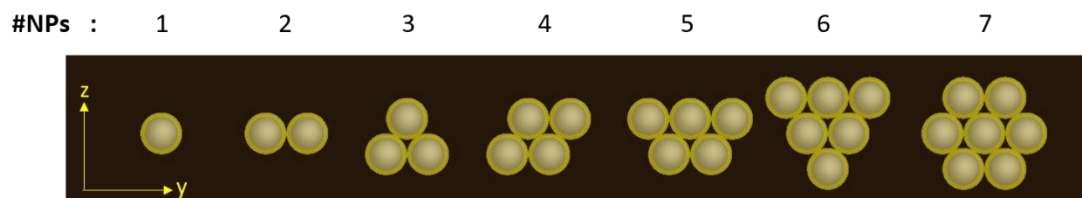
Figure S10. Schematic of the 3D-FDTD calculation.

Output parameters : scattering cross-section, absorption cross-section

- e.g. scattering cross-section



→ **Sample geometry**



Random polarization

= (x-polar result + y-polar result) / 2

Figure S11. Schematic of output parameters for 3D-FDTD calculation and geometry depending on the number of NPs.

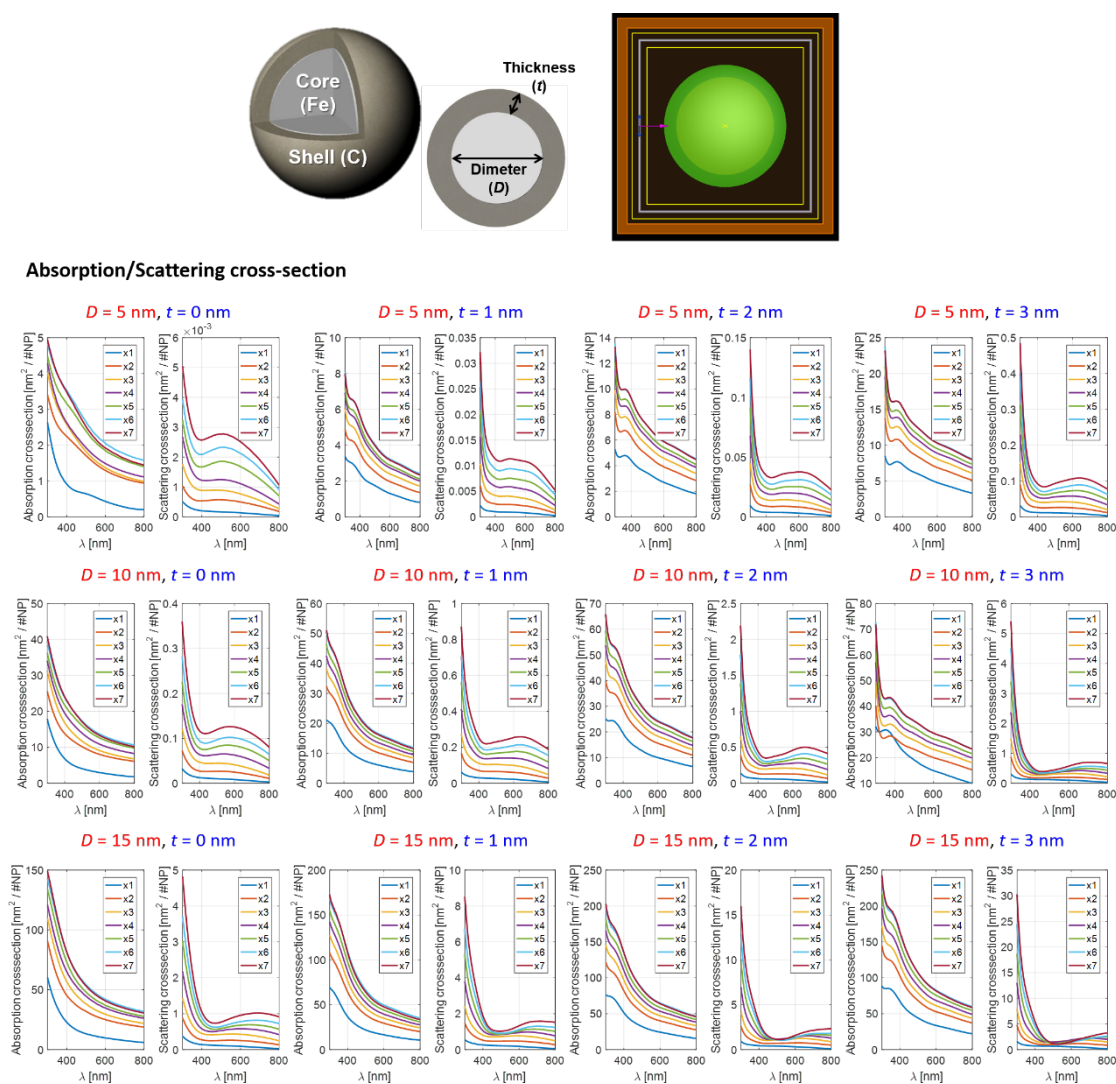
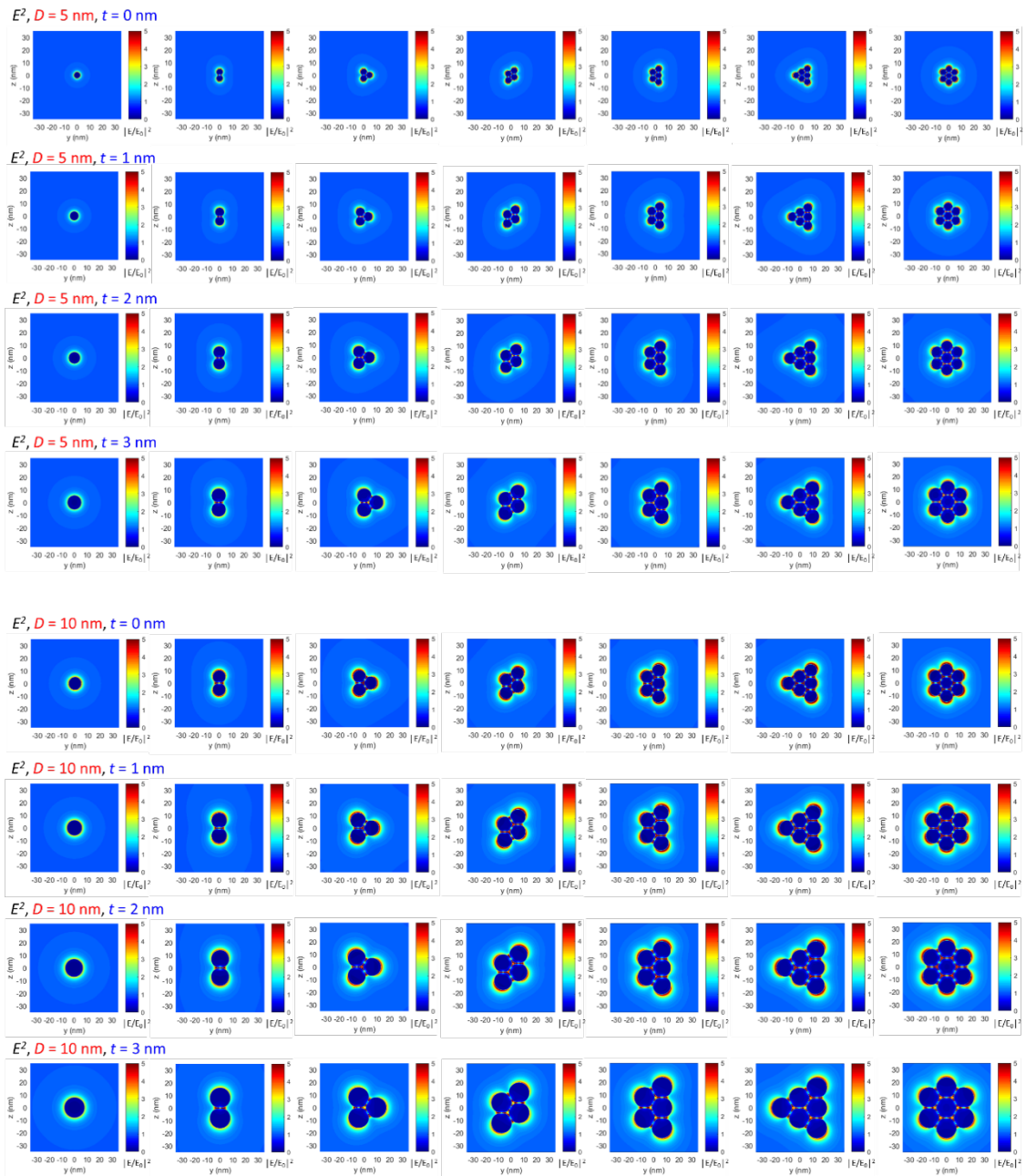


Figure S12. Absorption scattering cross-section graph through changes in the core diameter (D) of NPs and the thickness (t) of shells.



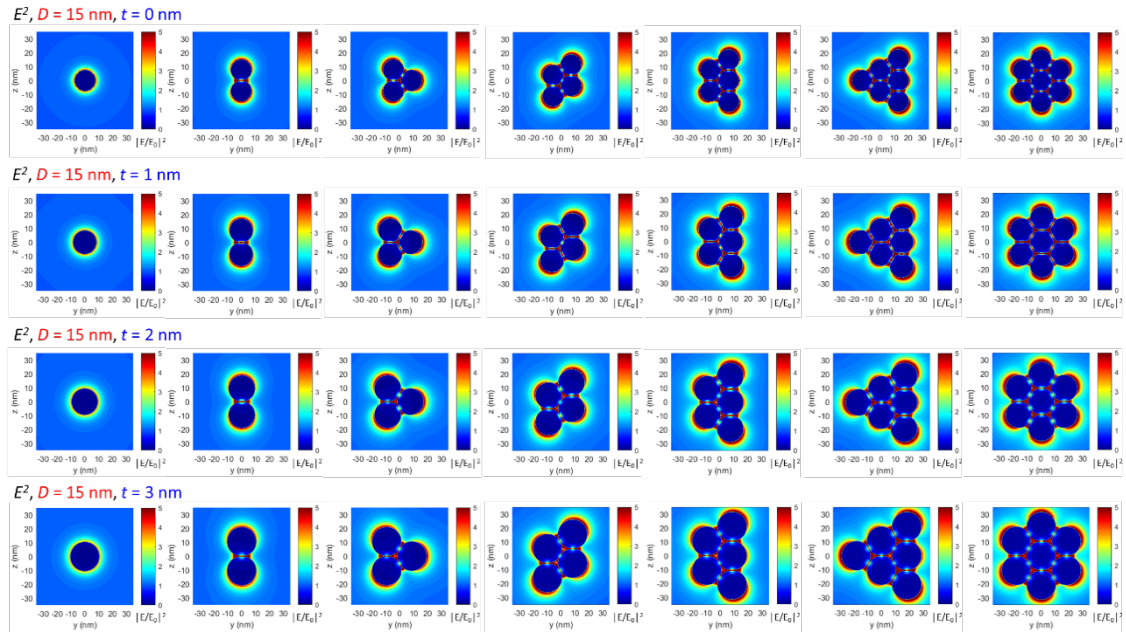


Figure S13. 3D-FDTD calculations: Electric field calculated according to the geometry of FeC@C NPs having the core diameter (D) and shell thickness (t) as variables.

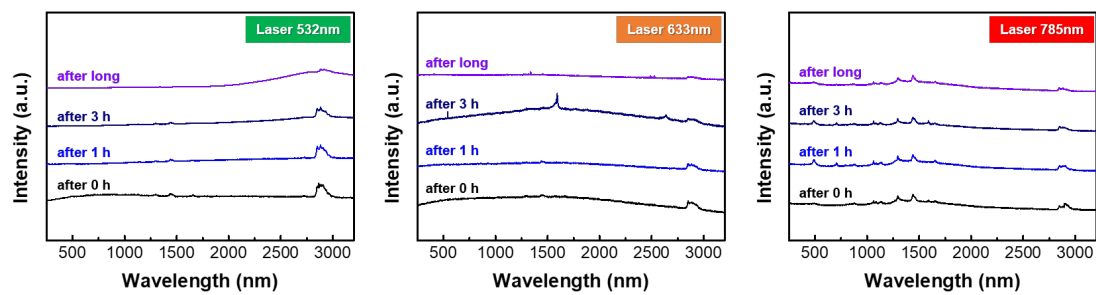


Figure S14. Raman spectra according to the waiting time for each laser (532, 633, and 785 nm).

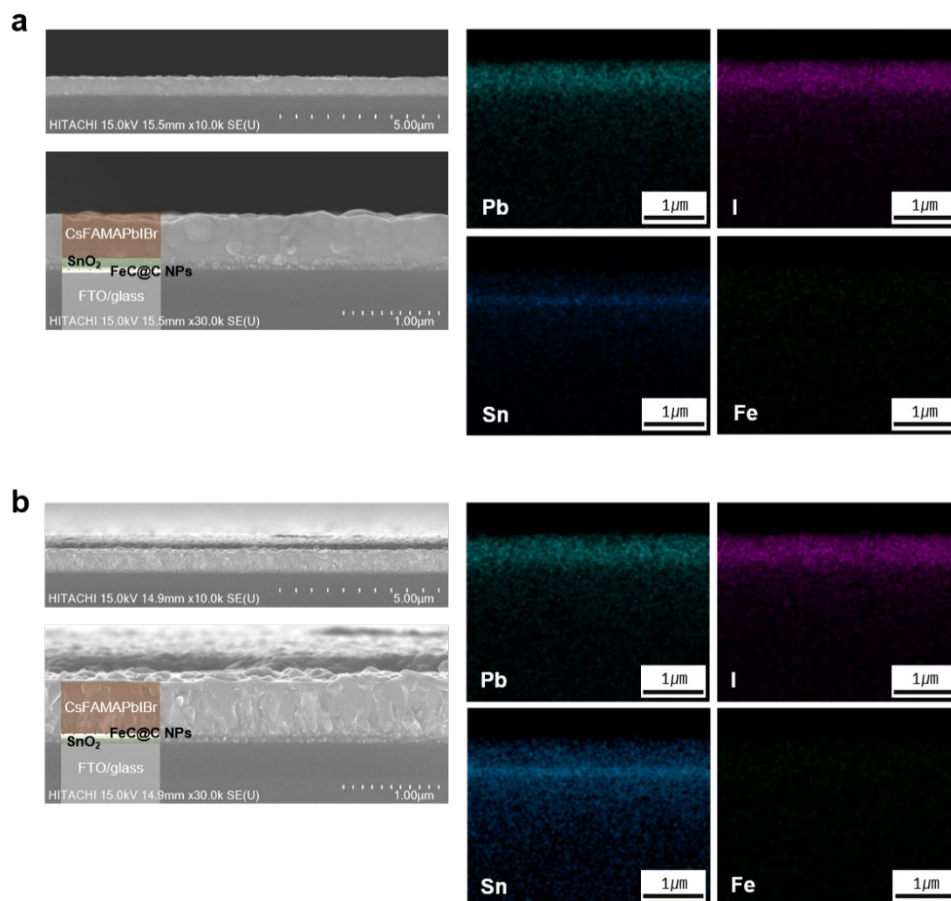


Figure S15. Cross-sectional SEM images and EDS of PSCs. a) SnO₂ on FeC@C NPs layer and b) FeC@C NPs on SnO₂ layer

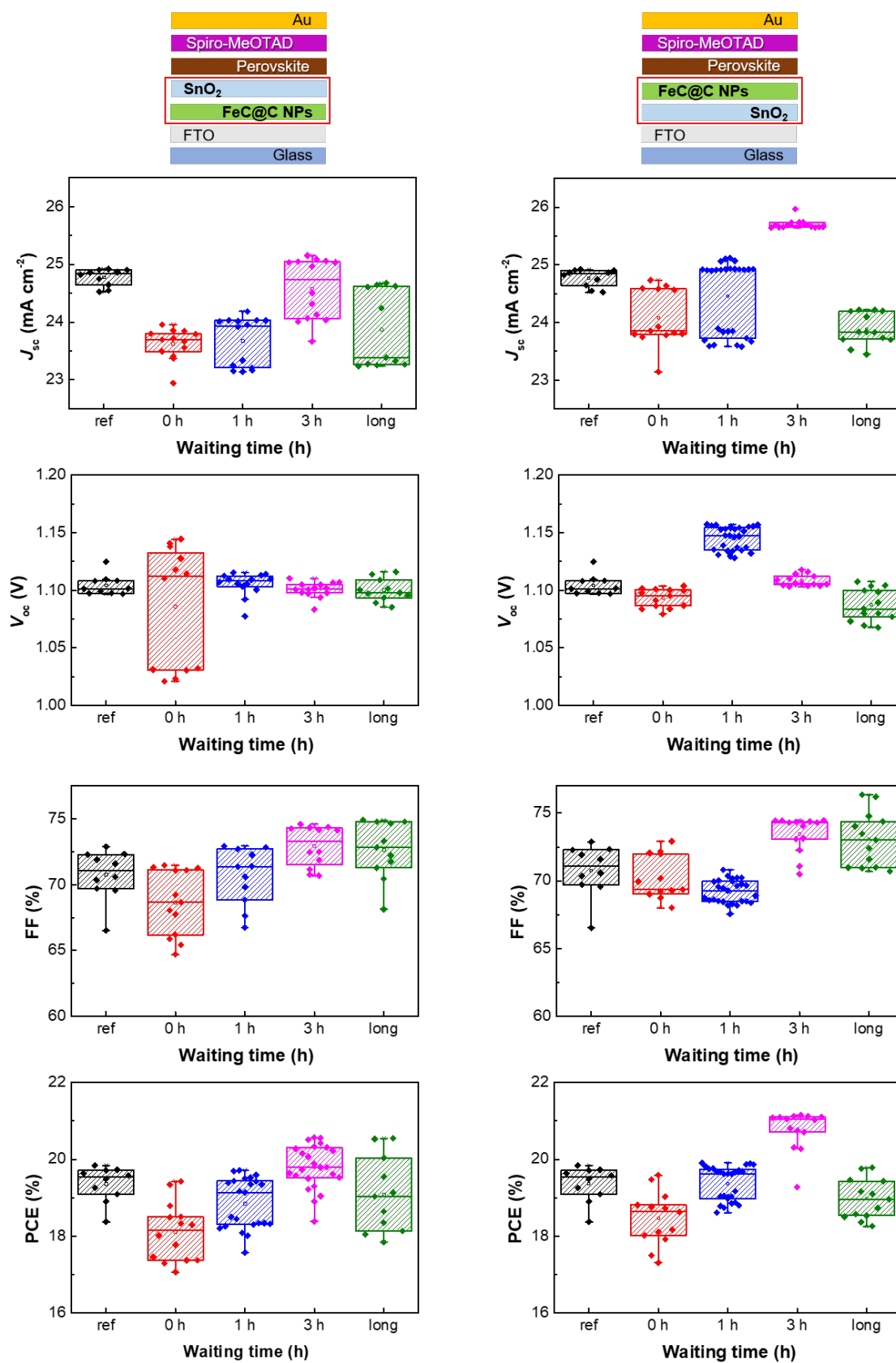


Figure S16. Statistical distribution of photovoltaic parameters for PSC devices.

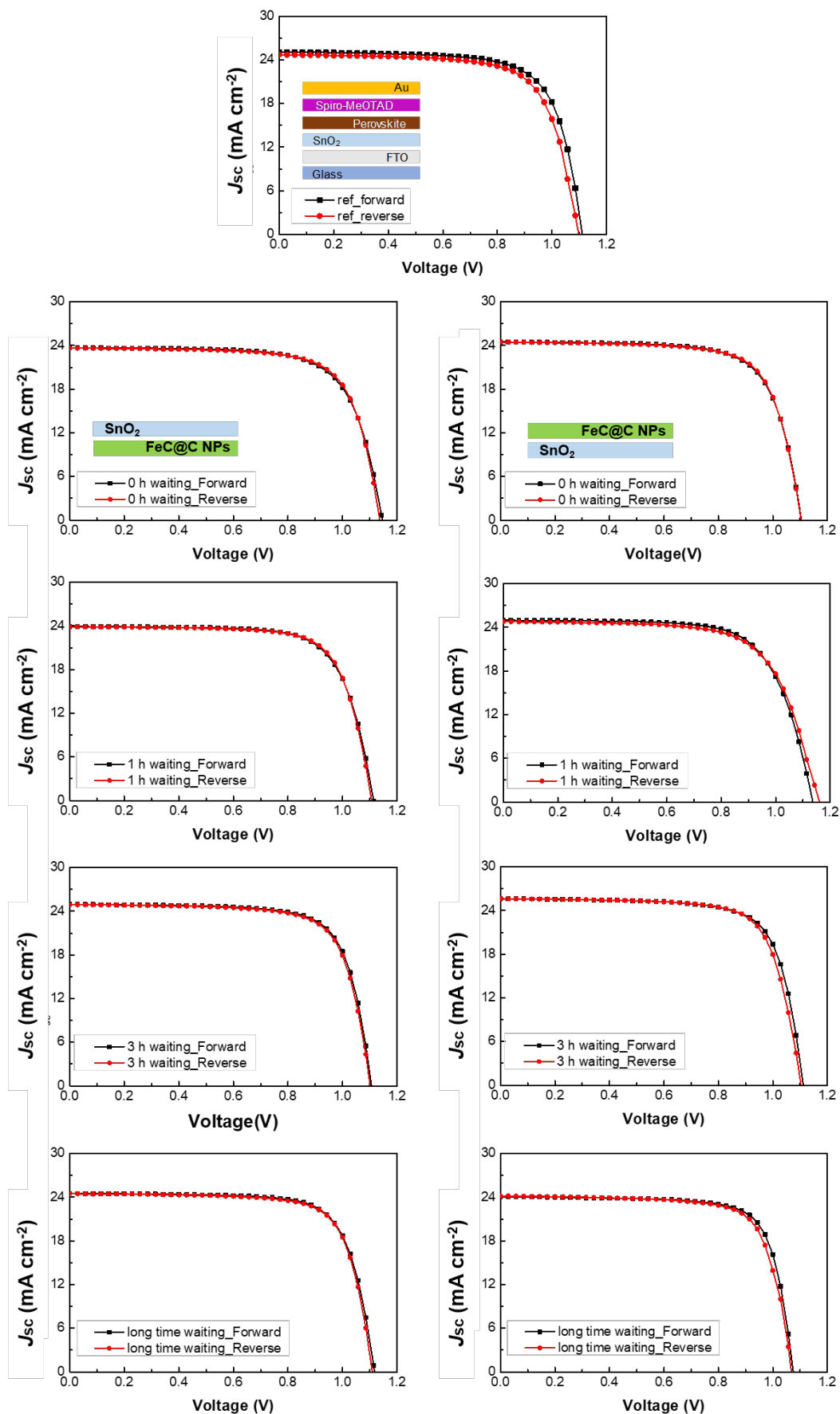


Figure S17. $J-V$ curves of optimized devices based on photovoltaic performance.

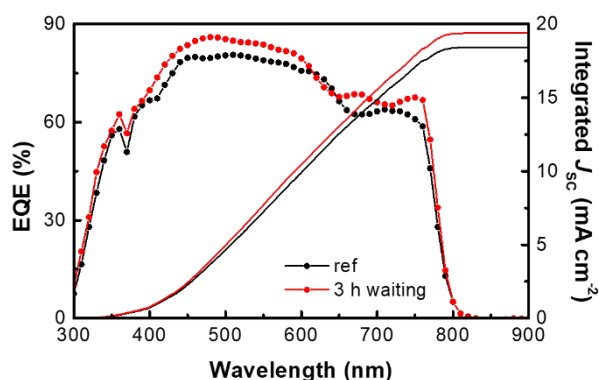


Figure S18. EQE spectra and Integrated J_{sc} of the performing PSCs: ref and after 3 h sample of FeC@C NPs on SnO₂ layer.

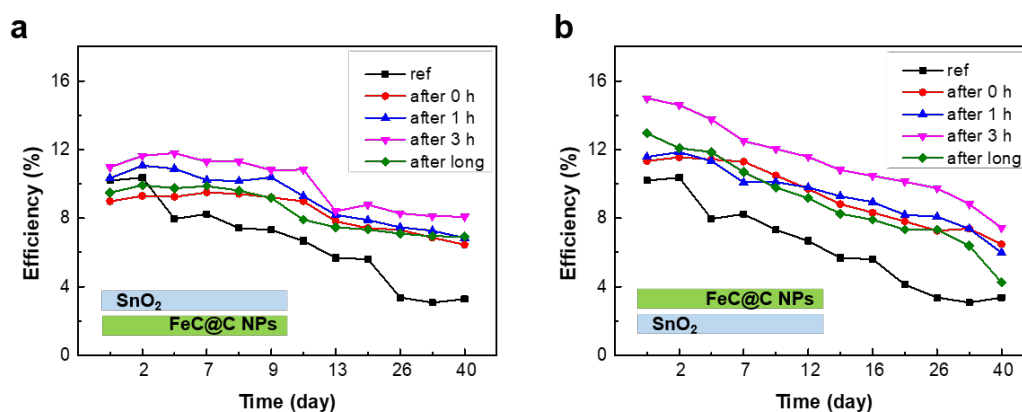


Figure S19. Long-term operating stability data of the PSCs. a) SnO₂ on FeC@C NPs layer and b) FeC@C NPs on SnO₂ layer.